Article

Immunity

# CD155 on Tumor Cells Drives Resistance to Immunotherapy by Inducing the Degradation of the Activating Receptor CD226 in CD8$^+$ T Cells

## Graphical Abstract

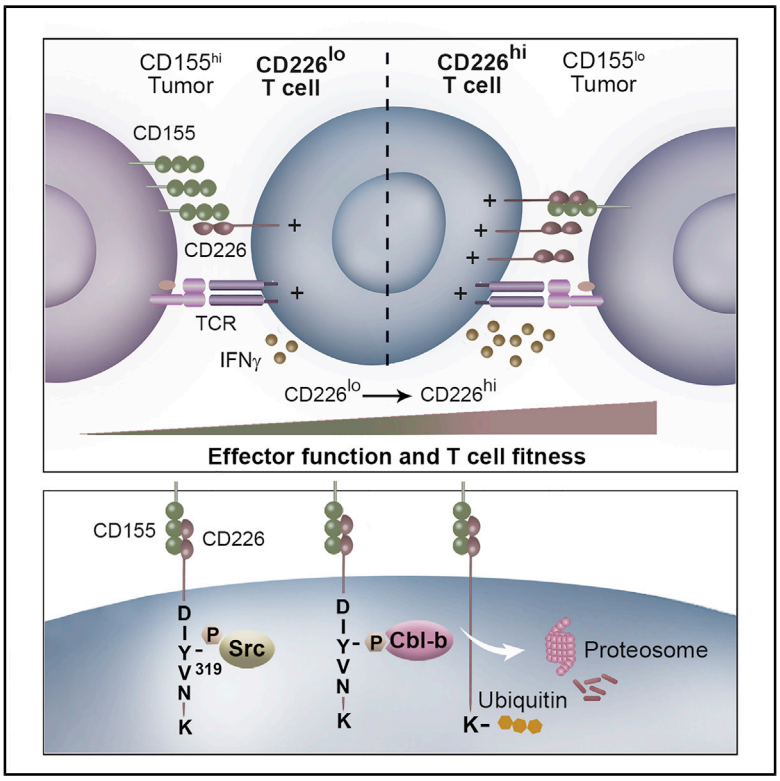


## Highlights

- Dysfunctional CD226-negative T cells accumulate in mouse and human tumors
- CD155 induces ubiquitination via CBL-B and proteasomal degradation of CD226
- A mutation of Y319 maintains CD226 expression and improves anti-tumor immunity
- ICB-therapy in melanoma patients relies on the presence of CD226$^+$CD8$^+$ T cells

## Authors

Matthias Braun, Amelia Roman Aguilera, Ashmitha Sundarrajan, ..., Ludovic Martinet, Mark J. Smyth, Tobias Bald

## Correspondence

mark.smyth@qimrberghofer.edu.au (M.J.S.), tobias.bald@qimrberghofer.edu.au (T.B.)

## In Brief

Braun et al. find that CD155 on tumor cells drives the proteasomal degradation of the activating receptor CD226 on tumor-infiltrating CD8$^+$ T cells, thus promoting immune evasion and resistance to cancer immunotherapy.

Braun et al., 2020, Immunity *53*, 805–823
October 13, 2020 
https://doi.org/10.1016/j.immuni.2020.09.010

CellPress

Immunity

CellPress

Article

# CD155 on Tumor Cells Drives Resistance to Immunotherapy by Inducing the Degradation of the Activating Receptor CD226 in CD8$^+$ T Cells

Matthias Braun,[1,2] Amelia Roman Aguilera,[1,28] Ashmitha Sundarrajan,[2,28] Dillon Corvino,[2] Kimberley Stannard,[1,2] Sophie Krumeich,[2] Indrajit Das,[1] Luize G. Lima,[3] Lizeth G. Meza Guzman,[4,5] Kunlun Li,[4,5] Rui Li,[6,7] Nazhifah Salim,[2] Maria Villancanas Jorge,[2] Sunyoung Ham,[3] Gabrielle Kelly,[1] Frank Vari,[1] Ailin Lepletier,[1] Ashwini Raghavendra,[1] Sally Pearson,[1] Jason Madore,[1] Sebastien Jacquelin,[9] Maike Effern,[10,11] Brodie Quine,[1,2] Lambros T. Koufariotis,[12] Mika Casey,[1] Kyohei Nakamura,[1] Eun Y. Seo,[13] Michael Hölzel,[10] Matthias Geyer,[14] Glen Kristiansen,[15] Touraj Taheri,[16]

*(Author list continued on next page)*

[1]Immunology in Cancer and Infection Laboratory, QIMR Berghofer Medical Research Institute, Herston, QLD, Australia
[2]Oncology and Cellular Immunology Laboratory, QIMR Berghofer Medical Research Institute, Herston, QLD, Australia
[3]Tumor Microenvironment Laboratory, QIMR Berghofer Medical Research Institute, Herston, QLD, Australia
[4]The Walter and Eliza Hall Institute of Medical Research, Parkville, VIC, Australia
[5]Department of Medical Biology, The University of Melbourne, Parkville, VIC, Australia
[6]Laboratory of Molecular Oncology, Institut de recherches cliniques de Montréal, Montréal, QC, Canada
[7]Department of Medicine, McGill University, Montréal, QC, Canada
[8]Department of Medicine, University of Montréal, Montréal, QC, Canada
[9]Gordon and Jessie Gilmour Leukemia Laboratory, QIMR Berghofer Medical Research Institute, Herston, QLD, Australia
[10]Institute of Experimental Oncology, Medical Faculty, University Hospital Bonn, University of Bonn, Bonn, Germany
[11]Department of Microbiology & Immunology, The University of Melbourne at the Peter Doherty Institute for Infection & Immunity, Melbourne, VIC, Australia
[12]Medical Genomics Laboratory, QIMR Berghofer Medical Research Institute, Herston, QLD, Australia
[13]Immuno-Oncology Discovery, Bristol-Myers Squibb, Redwood City, CA, USA
[14]Institute of Structural Biology, University Hospital Bonn, University of Bonn, Bonn, Germany
[15]Institute of Pathology, University Hospital Bonn, University of Bonn, Bonn, Germany
[16]Pathology Queensland, Royal Brisbane and Women's Hospital, University of Queensland Herston, Herston, QLD, Australia

*(Affiliations continued on next page)*

## SUMMARY

The activating receptor CD226 is expressed on lymphocytes, monocytes, and platelets and promotes anti-tumor immunity in pre-clinical models. Here, we examined the role of CD226 in the function of tumor-infiltrating lymphocytes (TILs) and resistance to immunotherapy. In murine tumors, a large proportion of CD8$^+$ TILs had decreased surface expression of CD226 and exhibited features of dysfunction, whereas CD226$^{hi}$ TILs were highly functional. This correlation was seen also in TILs isolated from HNSCC patients. Mutation of CD226 at tyrosine 319 (Y319) led to increased CD226 surface expression, enhanced anti-tumor immunity and improved efficacy of immune checkpoint blockade (ICB). Mechanistically, tumor-derived CD155, the ligand for CD226, initiated phosphorylation of Y319 by Src kinases, thereby enabling ubiquitination of CD226 by CBL-B, internalization, and proteasomal degradation. In pre-treatment samples from melanoma patients, CD226$^+$CD8$^+$ T cells correlated with improved progression-free survival following ICB. Our findings argue for the development of therapies aimed at maintaining the expression of CD226.

## INTRODUCTION

Cancer cells are able to escape destruction by the immune system by exploiting a plethora of immunosuppressive pathways (Schreiber et al., 2011). One such escape mechanism involves the induction of inhibitory receptors on tumor-infiltrating T cells, such as Programmed Death 1 (PD-1) and cytotoxic T-lymphocyte-associated protein 4 (CTLA-4) (Wherry and Kurachi, 2015). Antibody-mediated blockade of these receptors improves the outcome for cancer patients (Helmink et al., 2018). Driven by the clinical success of immune checkpoint blockade (ICB), research has focused on understanding the biology and utility

Elizabeth Ahern,[1,17] Brett G.M. Hughes,[17] James S. Wilmott,[18,19] Georgina V. Long,[18,19,20,21] Richard A. Scolyer,[18,22] Martin D. Batstone,[17] Jennifer Landsberg,[23] Dimo Dietrich,[24] Oltin T. Pop,[25] Lukas Flatz,[25,26] William C. Dougall,[1] André Veillette,[6,7,8] Sandra E. Nicholson,[4,5] Andreas Möller,[3] Robert J. Johnston,[13] Ludovic Martinet,[27] Mark J. Smyth,[1,29,*] and Tobias Bald[2,29,30,*]

[17]Royal Brisbane and Women's Hospital, University of Queensland Herston, Herston, QLD, Australia
[18]Melanoma Institute Australia, The University of Sydney, Sydney, NSW, Australia
[19]The University of Sydney, Central Clinical School, Sydney, NSW, Australia
[20]Royal North Shore Hospital, Sydney, NSW, Australia
[21]Mater Hospital, Sydney, NSW, Australia
[22]Royal Prince Alfred Hospital, Sydney, NSW, Australia
[23]Department of Dermatology and Allergy, University Hospital Bonn, University of Bonn, Bonn, Germany
[24]Department of Otolaryngology, Head and Neck Surgery, University Hospital Bonn, University of Bonn, Bonn, Germany
[25]Institute of Immunobiology, Kantonsspital St.Gallen, St.Gallen, Switzerland
[26]Department of Dermatology, Kantonsspital St.Gallen, St.Gallen, Switzerland
[27]Institut National de la Santé et de la Recherche Médicale (INSERM) UMR 1037, Cancer Research Center of Toulouse (CRCT), Toulouse F-31000, France
[28]These authors contributed equally
[29]These authors contributed equally
[30]Lead Contact
*Correspondence: mark.smyth@qimrberghofer.edu.au (M.J.S.), tobias.bald@qimrberghofer.edu.au (T.B.)
https://doi.org/10.1016/j.immuni.2020.09.010

of inhibitory receptors (O'Donnell et al., 2019; Thommen and Schumacher, 2018). In addition to inhibitory receptors, fine-tuning of T cell responses also occurs through a myriad of activating receptors expressed on the surface of T cells. Although agonistic antibodies targeting some activating receptors are under evaluation, our knowledge of the regulation and expression patterns of activating receptors in the tumor microenvironment (TME) is limited (Attanasio and Wherry, 2016).

One of these activating receptors is CD226 (DNAX Accessory Molecule-1, DNAM-1, PTA-1, TLiSA1), a transmembrane protein of the immunoglobulin (Ig) superfamily (Burns et al., 1985). CD226 acts as an adhesion molecule to promote the cytotoxic function of lymphocytes (Shibuya et al., 1996). CD226 is expressed on T cells, natural killer (NK) cells, B cells, monocytes, and platelets (Lepletier et al., 2019; Martinet and Smyth, 2015; Shibuya et al., 1996; Vo et al., 2016) and competes with the inhibitory receptors TIGIT and CD96 (Chan et al., 2014; Johnston et al., 2015; Pauken and Wherry, 2014) for binding to Nectin-like molecule 5 (Necl-5, PVR, CD155) and in humans to Nectin-2 (CD112), although with lower affinity to the latter (Bottino et al., 2003; Tahara-Hanaoka et al., 2004). Both ligands are expressed on the surface of activated antigen-presenting, stressed, virus-infected, and cancer cells (Ardolino et al., 2011; Bottino et al., 2003; Kamran et al., 2013; Li et al., 2018). In addition to its two extracellular Ig-like domains, CD226 has two conserved phosphorylation sites in its cytosolic domain at tyrosine 319 (Y319) and serine 326 (S326) in mice and at Y322 and S329 in humans. Whereas both phosphorylation sites are thought to contribute to immune cell function, a detailed understanding of CD226 signaling remains elusive.

CD226 is an important NK cell-activating receptor implicated in the killing of tumor cells and control of viruses (Lakshmikanth et al., 2009; Nabekura et al., 2014). Phosphorylation of Y319 on CD226 is critical for mouse NK cell activation and cytotoxicity *in vitro*, unlike S326 phosphorylation (Zhang et al., 2015). Phosphorylation at S329 is required for CD226 co-localization on lipid rafts with LFA-1 in human CD4$^+$ T cells (Shibuya et al., 1998; 1999; 2003; Shirakawa et al., 2005). This interaction is thought to be important for the formation and stability of the immunological synapse in NK and T cells (Hou et al., 2014; Kim et al., 2017; Ramsbottom et al., 2014; Shibuya et al., 1999; Shirakawa et al., 2006). CD226 can also amplify T cell receptor (TCR) signaling in human CD4$^+$ T cells via enhanced phosphorylation of Vav-1 (Gaud et al., 2018). Although we and others have shown that *Cd226*$^{-/-}$ mice have impaired tumor control, the importance of CD226 for cancer immunotherapy remains elusive (Croxford et al., 2013; Gilfillan et al., 2008; Iguchi-Manaka et al., 2008; Tahara-Hanaoka et al., 2006).

Here, we employed mouse tumor models and pre-ICB treatment melanoma patient samples to interrogate the regulation and function of CD226 in tumor immunity and to assess its relevance in the efficacy of immunotherapy. Our findings point to a negative feedback mechanism wherein tumor-derived CD155 induces the internalization and degradation of CD226 leading to the accumulation of dysfunctional CD8$^+$ T cells and resistance to cancer immunotherapy.

## RESULTS

### CD226-Negative Tumor-Infiltrating CD8$^+$ T Cells Are Dysfunctional

As opposed to most other activating receptors, CD226 is homogeneously expressed on naive (Tn) and central memory (Tcm) CD8$^+$ T cells in mice, whereas only a small proportion of effector memory (Tem) CD8$^+$ T cells were found to be CD226 negative (Figure S1A). However, upon TCR stimulation of splenic CD8$^+$ T cells, CD226 surface expression was uniformly increased (Figure 1A). In line with our previous findings (Gilfillan et al., 2008), we confirmed that subcutaneously (s.c.) transplanted tumors grew faster in *Cd226*$^{-/-}$ mice (Figures S1B–S1I). Flow cytometric analyses showed reduced frequencies of CD8$^+$ and CD8$^+$IFN$\gamma^+$ T cells infiltrating tumors in *Cd226*$^{-/-}$ mice compared to wild-type (WT) mice (Figures S1C and S1E). This prompted us to study CD226 surface expression in CD8$^+$ TILs isolated from

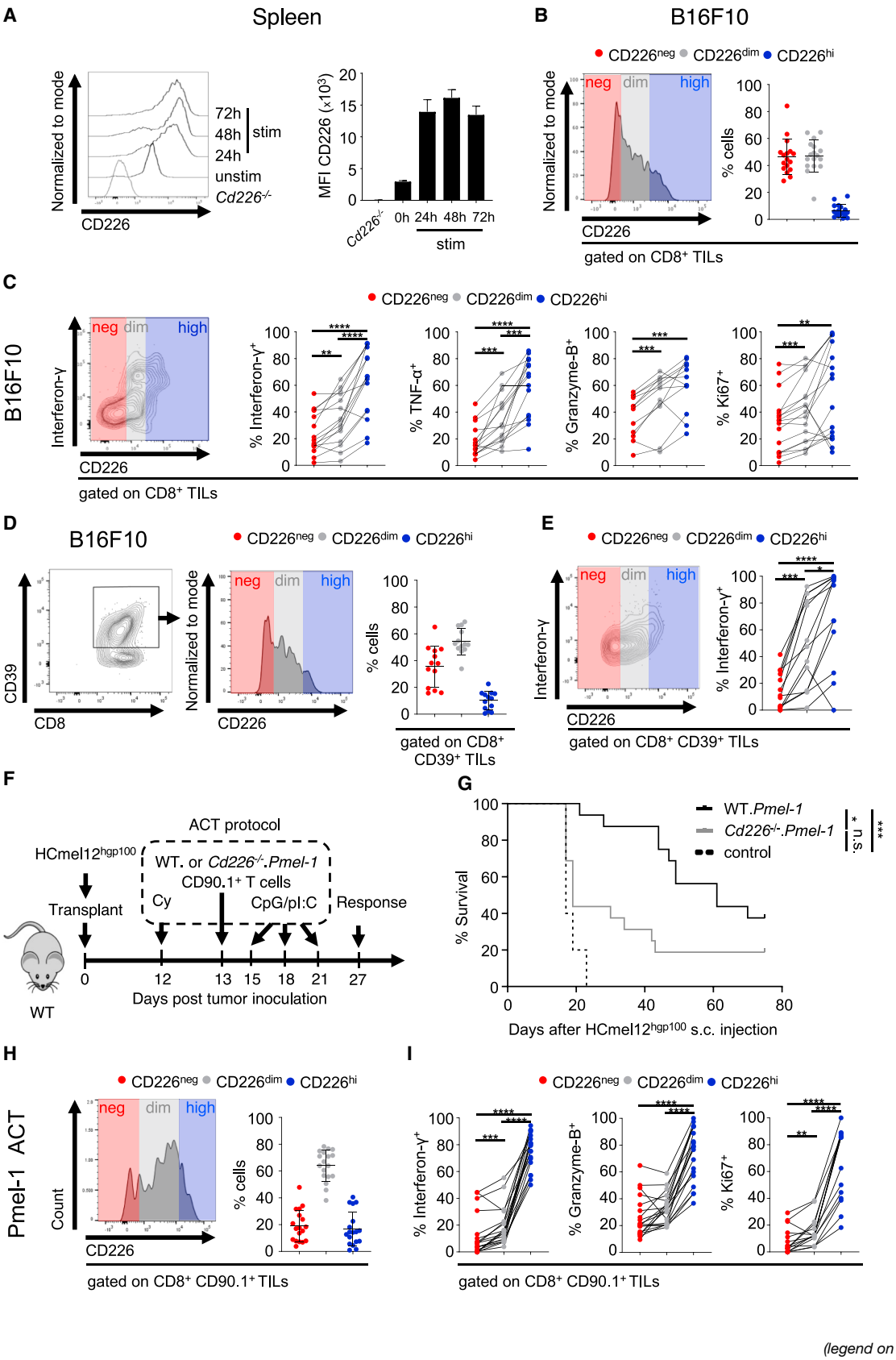


*(legend on next page)*

WT mice. A large proportion of CD8$^+$ TILs were CD226 negative (CD226$^{neg}$), a second subset expressed intermediate levels of CD226 (CD226$^{dim}$), similar to resting T cells, and a third subset expressed high levels of CD226 (CD226$^{hi}$) similar to *in vitro* activated splenic CD8$^+$ T cells (Figure 1B and S1D–S1J). Given that CD226 is an activating receptor, we hypothesized that CD226 surface expression correlated with T cell fitness. Indeed, we found an association between CD226 surface expression and the capability of *ex vivo* restimulated CD8$^+$ T cells isolated from B16F10 or MC38 tumors to produce effector cytokines and granzyme B and to proliferate as indicated by Ki67 staining (Figure 1C, S1K, and S1L). Since CD226$^{neg}$ T cells displayed a dysfunctional phenotype, we assessed co-expression of CD226 and inhibitory receptors on CD8$^+$ TILs isolated from B16F10 melanoma. Inhibitory receptor expression increases upon T cell activation, associates with loss of effector function, and defines exhausted T cells (Tex) (Thommen and Schumacher, 2018; Wherry and Kurachi, 2015). Recently, the ATP ecto-nucleotidase CD39 was reported to identify Tex cells (Gupta et al., 2015; Canale et al., 2018; Thelen et al., 2018). Only a small proportion of CD39-, PD-1-, LAG3-, TIGIT-, TIM-3-, or CD96-expressing CD8$^+$ TILs were negative for CD226 (Figure 1D, S2A, and S2B). Interestingly, interferon-$\gamma$ (IFN$\gamma$) production correlated with CD226 expression even in CD8$^+$CD39$^+$, CD8$^+$PD-1$^+$CD39$^+$, and CD8$^+$PD-1$^+$Tim-3$^+$ TILs (Figure 1E, S2C, and S2D).

In the absence of a conditional CD226 mouse model, we adoptively transferred WT.*Pmel-1* or *Cd226*$^{-/-}$.*Pmel-1* T cells into melanoma-bearing WT mice. WT mice were s.c. injected with mouse melanoma HCmel12$^{hgp100}$ cells (Bald et al., 2014) and engineered to express the high-affinity human antigen hgp100 recognized by Pmel-1 T cells (Effern et al., 2020). Once tumors reached ~5 mm in diameter, mice were preconditioned with cyclophosphamide and received either WT.*Pmel-1* or *Cd226*$^{-/-}$.*Pmel-1* T cells followed by innate immune stimulation (Glodde et al., 2017; Landsberg et al., 2012) (Figure 1F). Adoptive cell transfer (ACT) of WT.*Pmel-1* T cells induced robust anti-tumor immunity and prolonged survival (Figure 1G). In contrast, *Cd226*$^{-/-}$.*Pmel-1* T cells only slightly improved the survival of mice compared to untreated controls, highlighting the importance of CD226 expression in CD8$^+$ T cells for anti-tumor immunity and ACT. TIL analysis showed that CD226 expression varies also in antigen-specific T cells. We found CD226$^{neg}$, CD226$^{dim}$, and CD226$^{hi}$ subsets as early as 10 days after ACT of WT.*Pmel-1* T cells (Figure 1H). CD226 surface expression correlated with T cell fitness evidenced by intracellular staining for IFN$\gamma$, Granzyme-B, Ki67, TNF$\alpha$, and Bcl-2 (Figures 1I and S2E). Only a small proportion of PD-1-, TIGIT-, or TIM-3-expressing antigen-specific Pmel-1 TILs were negative for CD226; still, IFN$\gamma$ production correlated with CD226 expression (Figures S2F–S2I), supporting the idea that loss of CD226 represents a complementary mechanism for T cell dysfunction in addition to induction of inhibitory receptors.

## Genes Associated with Effector Function and Immunological Synapse Formation Are Enriched in CD226$^{hi}$ T Cells

To investigate the transcriptional differences between CD226$^{hi}$ and CD226$^{neg}$ tumor-infiltrating antigen-specific T cells, we utilized single-cell RNA-sequencing (scRNA-seq) in conjunction with cellular indexing of transcriptomes and epitopes by sequencing (CITE-seq) technology. Leveraging the CITE-seq technology allowed the simultaneous detection of mRNA and CD226 protein expression using oligo-labeled antibodies (Stoeckius et al., 2017). Pmel-1 T cells were adoptively transferred into HCmel12$^{hgp100}$ melanoma-bearing WT mice. On day 12 after ACT, TILs were stained with an anti-CD226 CITE-seq antibody and Pmel-1 T cells were isolated. After cell lysis, cellular mRNA and the CD226 antibody-derived tags (CD226-ADT) were indexed by a shared cellular barcode and sequenced (Figure 2A). Consistent with previous flow cytometric data, the expression profile of captured CD226-ADT, recapitulated the presence of CD226$^{neg}$, CD226$^{dim}$, and CD226$^{hi}$ populations (Figure 2B). The expression of *Cd226* mRNA partially correlated (r = 0.57) with CD226-ADT abundance across the defined populations or at a per cell basis (Figures 2C and 2D).

Differential gene expression analysis showed large transcriptional differences between CD226$^{neg}$ and CD226$^{hi}$ T cells as defined by CD226-ADT expression, while CD226$^{dim}$ T cells showed an intermediate profile (Figure 2E). Concordant with flow cytometric data, transcriptional profiling revealed an

**Figure 1. Tumor-Infiltrating CD226$^{neg}$CD8$^+$ T Cells Are Dysfunctional**

(A) Histograms showing CD226 expression in splenic CD8$^+$ T cells isolated from *Cd226*$^{-/-}$ or WT mice treated as indicated (left) and CD226 MFI (right, n = 7 (WT), mean ± SD, cumulative of two experiments).

(B) Histogram showing CD226 expression on CD8$^+$ TILs isolated 14 days after B16F10 injection into WT mice (left) and quantification of CD226 subsets (right, n = 15, mean ± SD, cumulative of three experiments).

(C) Contour plot showing CD226 and IFN$\gamma$ in CD8$^+$ TILs from B16F10 tumors (left) and quantification of IFN$\gamma^+$, TNF$\alpha^+$, Granzyme-B$^+$, and Ki67$^+$ in CD8$^+$ TILs from B16F10 across CD226 subsets (right, n = 15 for IFN$\gamma$ and TNF$\alpha$, n = 12 for GrzB, n = 10 for Ki67, cumulative of two experiments).

(D) Contour plot showing CD226 and CD39 expression in CD8$^+$ TILs from B16F10 tumors (left) and quantification of CD226 subsets (right, n = 13, mean ± SD, cumulative of two experiments).

(E) Contour plot showing CD226 and IFN$\gamma$ in CD8$^+$CD39$^+$TILs from B16F10 tumors (left) and quantification of IFN$\gamma^+$ in CD8$^+$CD39$^+$TILs across indicated CD226 subsets (right, same experiments as D).

(F) Protocol for ACT of HCmel12$^{hgp100}$-bearing WT mice with WT. or *Cd226*$^{-/-}$.*Pmel-1* T cells. (Cy, cyclophosphamide).

(G) Kaplan-Meier survival curves for mice treated as indicated (n = 5 for control, n = 6 for WT. and *Cd226*$^{-/-}$.*Pmel-1*; experiment done once for control and cumulated from two ACT experiments).

(H) Histogram showing CD226 expression in CD8$^+$CD90.1$^+$TILs from HCmel12$^{hgp100}$ bearing WT mice 7–10 days after ACT of WT.*Pmel-1* T cells (left) and quantification of CD226 subsets (right, n = 18, mean ± SD, cumulative of two experiments).

(I) Quantification of IFN$\gamma^+$, Granzyme-B$^+$, and Ki67$^+$ in Pmel-1 TILs 7–10 days after ACT across indicated CD226 subsets (right, n = 19 for IFN$\gamma$ and GrzB, n = 15 for Ki67, cumulative of two experiments).

Statistics: repeated-measure (RM) one-way ANOVA with post hoc Tukey's for multiple comparisons (C, E, and I), log-rank (Mantel-Cox) test for survival curves (G); *p < 0.05, **p < 0.01, ***p < 0.001, ****p < 0.0001.

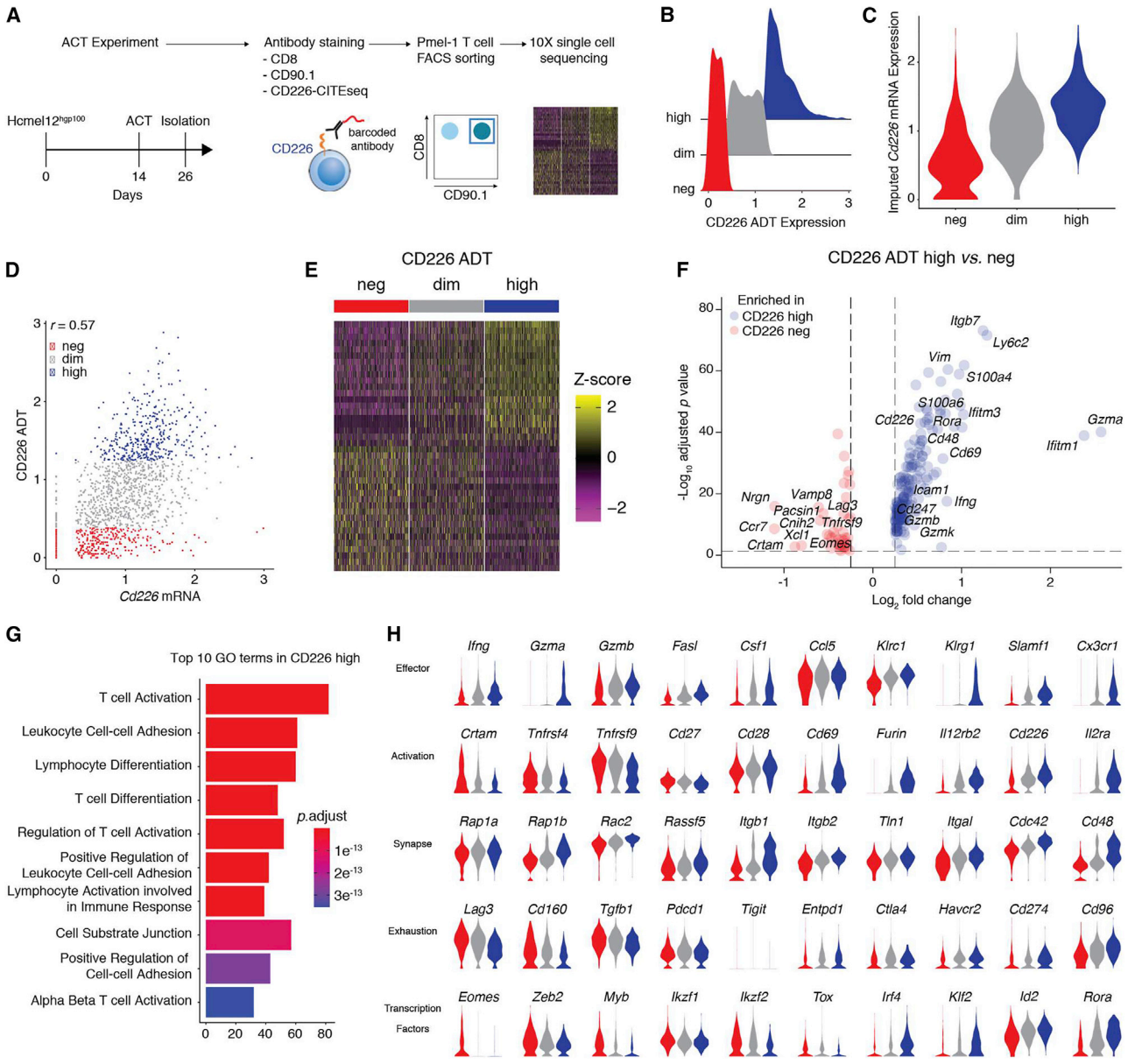


**Figure 2. Tumor Infiltrating CD226$^{hi}$ versus CD226$^{lo}$ CD8$^{+}$ T Cells Have a Distinct Transcriptional Profile**

(A) Experimental setup.

(B) Ridge plot showing CD226 protein expression as determined by CD226-CITE-seq antibody-derived tag (ADT) signals across CD226 subsets.

(C) Violin plot of imputed *Cd226* mRNA expression across CD226-ADT subsets.

(D) Scatterplot of imputed *Cd226* mRNA versus CD226-ADT expression.

(E) Heatmap of the top 20 differentially regulated genes of CD226$^{hi}$ (upper section) and CD226$^{lo}$ subsets (lower section) across CD226-ADT subsets (*adj*.p < 0.05).

(F) Volcano plot of differentially expressed genes in CD226$^{hi}$ versus CD226$^{lo}$ ADT subsets (*adj.p* < 0.05 and a $\log_2$ fold change >0.25 or <−0.25).

(G) Bar plot showing the top 10 GO terms in CD226$^{hi}$ cells (*adj.p* < 0.05).

(H) Violin plots showing the imputed mRNA expression of indicated genes across color coded CD226-ADT subsets (red = CD226$^{neg}$, gray = CD226$^{dim}$, blue = CD226$^{hi}$).

increase expression of genes involved in T cell activation (*Cd69*, *Il2ra)* and cytotoxicity (*Ifng*, *Grzb*) in CD226$^{hi}$ T cells (Figure 2F). Gene ontology (GO) analysis showed that gene sets for T cell activation, differentiation, and adhesion were enriched in CD226$^{hi}$ T cells (Figure 2G). Indeed, genes important for immunological synapse (IS) formation such as *Itgb2* (CD18) and *Itgal* (CD11a) (both form LFA-1) were increased in CD226$^{hi}$ T cells (Figure 2H). Additionally, the expression of genes encoding for small GTPases *Rap1a* and *Rap1b,* which are known to interact with LFA-1 and are implicated in TCR signaling and IS-formation (Raab et al., 2010), was higher in CD226$^{hi}$ T cells (Figure 2H).

Expression of inhibitory molecules was largely unaltered across CD226 subpopulations. However, *Lag3*, *Cd160*, and *Tgfb1* were enriched in the CD226$^{neg}$ population (Figure 2H).

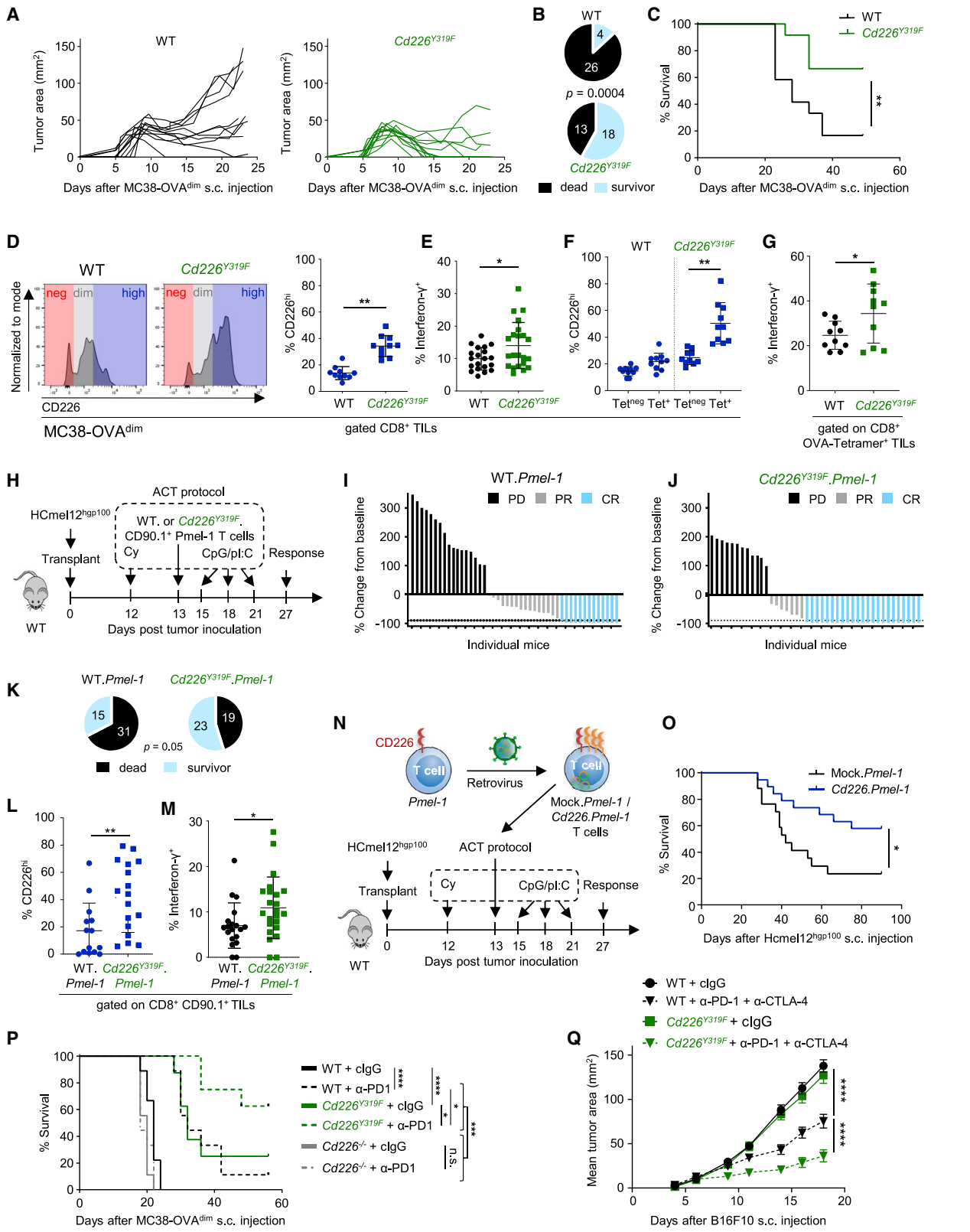


(legend on next page)

Interestingly, the costimulatory receptors *Crtam*, *Tnfrsf4*, and *Tnfrsf9* were also higher expressed in CD226$^{neg}$ cells (Figure 2H). The transcription factors *Rora*, *Id2*, *Klf2*, and *Irf4* were increased in CD226$^{hi}$ T cells. Conversely, CD226$^{neg}$ cells showed higher expression of *Eomes*, *Zeb2*, and *Myb* (Figure 2H). In summary, scRNA-seq analysis showed transcriptomic differences between CD226 populations. These observations support the notion that CD226 expression delineates a functional subset of T cells and that CD226 negativity is associated with a decreased effector transcriptional program.

## The Mutation *Cd226$^{Y319F}$* Leads to Increased CD226 Expression and Superior Anti-tumor Immunity and Immunotherapy

Zhang et al. (2015) previously showed that CD226 signaling via Y319 was essential for NK cell killing *in vitro*, but the importance of Y319 in T cells was unknown. To assess the role of Y319 for T cell-mediated anti-tumor immunity, we used a mouse strain harboring the point mutation *Cd226$^{Y319F}$*, which abrogates phosphorylation of Y319 (Zhang et al., 2015). This mutation did not affect immune cell development as we found no differences in various lymphocyte populations in healthy *Cd226$^{Y319F}$* mice compared to WT mice (Figures S3A–S3C). Extending and complementing previously published findings (Zhang et al., 2015), *Cd226$^{Y319F}$* mice showed a higher susceptibility to NK cell-dependent methylcholanthrene (MCA)-induced carcinogenesis, RMA-S challenge, and experimental metastasis compared to WT controls (Figures S3D–S3J). Of note, *Cd226$^{-/-}$* mice showed impaired tumor control compared to *Cd226$^{Y319F}$* mice, suggesting that phosphorylation of Y319 only partially contributes to NK cell-mediated tumor immunity *in vivo*.

To assess the importance of Y319 in T cell-mediated tumor-immunity, we injected immunogenic variants of MC38 colon carcinoma cells expressing moderate (MC38-OVA$^{dim}$) or high levels (MC38-OVA$^{hi}$) of the prototypic T cell antigen ovalbumin (OVA) into WT or *Cd226$^{Y319F}$* mice. As both models showed accelerated growth in CD8-depleted (Gilfillan et al., 2008) and *Cd226$^{-/-}$* mice (Figures S1D and S1G), they are ideal models to study the importance of CD226-Y319 signaling in tumor immunity. We observed reduced tumor growth and higher rates of MC38-OVA$^{dim}$ tumor rejection in *Cd226$^{Y319F}$* mice when compared with WT mice, which resulted in a prolonged survival (Figures 3A–3C). When we injected MC38-OVA$^{hi}$ tumors into WT and *Cd226$^{Y319F}$* mice, all tumors were initially rejected in both groups. However, although tumors frequently relapsed in WT mice (26/57), recurrence was reduced in *Cd226$^{Y319F}$* mice (9/52) resulting in prolonged survival (Figures S4A–S4C). *Cd226$^{Y319F}$* mice injected with Vk12598, multiple myeloma cells also showed improved tumor control and prolonged survival compared to WT mice, highlighting the importance of CD226 for the control of both solid and hematological cancers (Figure S4D).

To understand why mutation of Y319 led to improved tumor control, we analyzed the phenotype of CD8$^+$ TILs. We found higher frequencies of CD226$^{hi}$CD8$^+$ T cells and conversely reduced frequencies of CD226$^{neg}$CD8$^+$ T cells infiltrating tumors in *Cd226$^{Y319F}$* compared to WT mice (Figures 3D and S4E). In support of our hypothesis that CD226 expression correlated with improved effector function, we observed increased frequencies of IFN$\gamma^+$CD8$^+$ TILs in *Cd226$^{Y319F}$* mice (Figure 3E). We next assessed CD226 surface expression and effector function in OVA-specific (Tet$^+$) and non-specific (Tet$^{neg}$) CD8$^+$ TILs (Figure S4F). Although the frequency of CD226$^{hi}$ cells was comparable between both Tet$^+$ and Tet$^{neg}$ T cell subsets in WT mice, we found increased frequencies of CD226$^{hi}$ cells in Tet$^+$ T cells in *Cd226$^{Y319F}$* mice (Figure 3F). Additionally, a larger proportion of Tet$^+$ T cells from *Cd226$^{Y319F}$* mice were IFN$\gamma^+$ when compared with Tet$^+$ T cells from WT mice (Figure 3G). In concordance,

**Figure 3. A Point Mutation at Y319 Maintains CD226 Surface Expression, Improves T Cell Function and the Efficacy of Cancer Immunotherapies**

(A) Individual growth curves of MC38-OVA$^{dim}$ tumors in WT and *Cd226$^{Y319F}$* mice (n = 11 WT and n = 12 *Cd226$^{Y319F}$* mice, representative of three experiments).
(B) Corresponding pie charts showing number of surviving and dead mice (n = 30 WT and n = 31 *Cd226$^{Y319F}$* mice, cumulative of three experiments).
(C) Corresponding Kaplan-Meier survival curves for experiment in (A).
(D) Histograms showing CD226 expression in CD8$^+$ TILs (left) and quantification of CD8$^+$CD226$^{hi}$TILs 6–9 days after injection of MC38-OVA$^{dim}$ (right, n = 10, mean ± SD, representative of two experiments).
(E) Flow cytometric quantification of IFN$\gamma^+$CD8$^+$ TILs (n = 18, mean ± SD, cumulative of two experiments).
(F) Flow cytometric quantification of CD8$^+$CD226$^{hi}$ cells in Tet$^{neg}$ and OVA-Tet$^+$ TILs in WT and *Cd226$^{Y319F}$* mice (right, n = 10, mean ± SD, representative of two experiments).
(G) Flow cytometric quantification of IFN$\gamma^+$ in CD8$^+$ Tet$^+$TILs (n = 10, mean ± SD, experiment done once).
(H) Experimental protocol for ACT with WT. or *Cd226$^{Y319F}$.Pmel-1* T cells. (Cy, cyclophosphamide).
(I and J) Waterfall plots showing percentage of change in HCmel12$^{hgp100}$ tumor area 14 days after ACT relative to pre-treatment (PD, progressive disease; PR, partial response; CR, complete response) for WT.*Pmel-1* (n = 46) (I) and *Cd226$^{Y319F}$.Pmel-1* T cells (n = 42) (J).
(K) Corresponding pie charts showing the number of surviving and dead mice (cumulative of three experiments, K and I; WT group includes mice from Figure 1G).
(L) Flow cytometric quantification of CD8$^+$CD90.1$^+$CD226$^{hi}$ TILs 8–12 days after transfer of indicated T cells (n = 14 WT. and n = 17 *Cd226$^{Y319F}$.Pmel-1*, mean ± SD, cumulative of two experiments).
(M) Quantification of IFN$\gamma^+$CD8$^+$CD90.1$^+$ WT. or *Cd226$^{Y319F}$.Pmel-1* T cells 10–14 days after transfer (n = 19 WT. and n = 23 *Cd226$^{Y319F}$.Pmel-1*, mean ± SD, cumulative of three experiments).
(N) Experimental layout for ACT with retrovirally transduced Pmel-1 T cells.
(O) Corresponding Kaplan-Meier survival curves (n = 17 for Mock. and n = 19 for *Cd226.Pmel-1*; cumulative of two experiments).
(P) Kaplan-Meier survival curves for WT, *Cd226$^{-/-}$*, and *Cd226$^{Y319F}$* mice bearing MC38-OVA$^{dim}$ tumors treated as indicated (n = 8-9, representative of two experiments).
(Q) Mean tumor growth of B16F10 melanoma in WT or *Cd226$^{Y319F}$* mice treated as indicated (n = 7–10, mean ± SEM, representative of two experiments).
Statistics: Fisher's exact test (B and K), log-rank (Mantel-Cox) test (C, O, and P), one-way ANOVA with post hoc Tukey's for multiple comparisons (D, F, and L), unpaired two-tailed Student's t test (E, G, and M), two-way ANOVA with post hoc Tukey's for multiple comparisons (Q); *p < 0.05, **p < 0.01, ***p < 0.001, ****p < 0.0001.

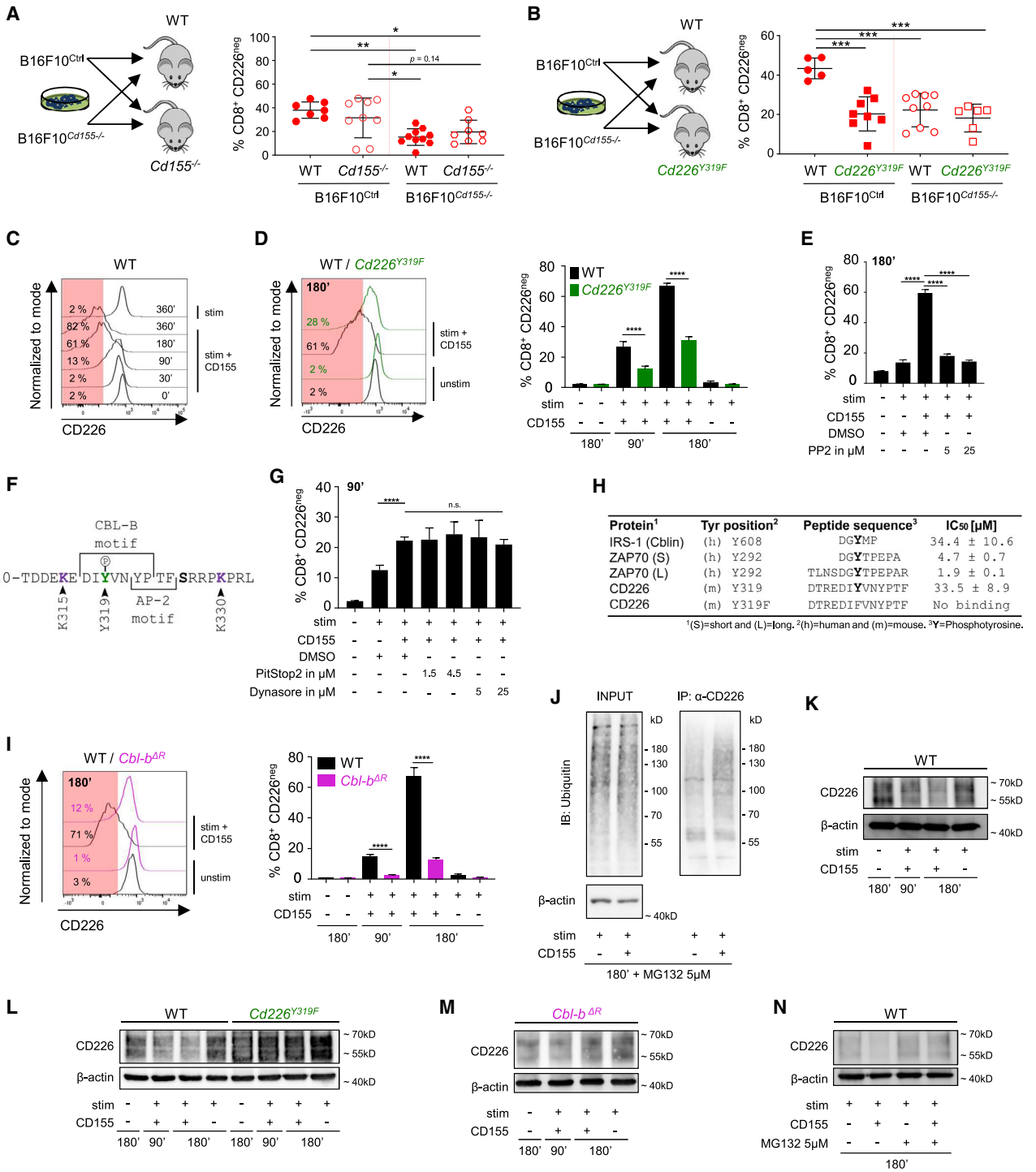


**Figure 4. CD155 Induces Y319 Phosphorylation, CBL-B Mediated Ubiquitination, and Proteasomal Degradation of CD226 in Mouse CD8$^+$ T Cells**

(A) Experimental setup (left) and flow cytometric quantification of CD8$^+$CD226$^{neg}$ TILs 10–14 days after injection (right, n = 7–9, mean ± SD, representative of three experiments).

(B) Experimental setup (left) and quantification CD8$^+$CD226$^{neg}$ TILs 10–14 days after injection (right, n = 5–9, mean ± SD, representative of two experiments).

(C) Representative histograms showing CD226 expression in splenic CD8$^+$T cells stimulated with CD3/CD28 (stim) ± CD155-coated beads.

(D) Representative histograms showing CD226 expression in splenic CD8$^+$ T cells from WT or *Cd226*$^{Y319F}$ mice (left); corresponding quantification (right, n = 3 spleens, mean ± SD, representative of two experiments).

(E) Quantification of CD226$^{neg}$CD8$^+$ T cells treated as indicated for 180 min (n = 3 spleens, mean ± SD, representative of two experiments).

*(legend continued on next page)*

we measured higher amounts of IFNγ protein in the TME of *Cd226*$^{Y319F}$ mice (Figure S4G).

To further address the role of Y319 in tumor-specific CD8$^+$ T cells, we generated *Cd226*$^{Y319F}$.*Pmel-1* mice. ACT with *Cd226*$^{Y319F}$.*Pmel-1* T cells was superior compared to WT.*Pmel-1* T cells, resulting in an increased number of complete responders and an increased number of long-term surviving mice (Figure 3H–3K). TIL analysis revealed that frequencies of CD226$^{hi}$ and IFNγ$^+$ Pmel-1 T cells were higher in mice treated with *Cd226*$^{Y319F}$ compared to WT.*Pmel-1* T cells (Figure 3L, 3M, and S4H). As CD226 surface expression in CD8$^+$ T cells was associated with superior fitness and tumor control, we hypothesized that overexpression of CD226 might be a rational strategy to improve ACT. For this, we transduced WT.*Pmel-1* T cells with control (MOCK.*Pmel-1*) or *Cd226*-encoding retroviral vectors (*Cd226*.*Pmel-1*) prior to ACT (Figure 3N). Indeed, ACT with *Cd226*.*Pmel-1* T cells improved the survival of melanoma-bearing mice compared to mice treated with MOCK.*Pmel-1* T cells (Figure 3O).

Next, we assessed the importance of CD226 surface expression for the efficacy of ICB therapy. Here, WT, *Cd226*$^{-/-}$, or *Cd226*$^{Y319F}$ mice were injected with MC38-OVA$^{dim}$ cells and treated with anti-PD1 ICB. While *Cd226*$^{-/-}$ mice completely failed to mount an anti-tumor response, *Cd226*$^{Y319F}$ mice treated with control IgG (cIgG) showed a similar response to WT mice treated with anti-PD1. *Cd226*$^{Y319F}$ mice treated with anti-PD-1 had the best survival (Figure 3P). Similar phenotypes were observed in the Hepa1-6 model (Figure S4I). Antibody-mediated blockade of CD226 during ICB treatment, also abrogated the therapeutic efficacy of ICB (Figure S4J). The importance of CD226 for ICB was further highlighted by improved efficacy of anti-PD1 + anti-CTLA4 combination ICB in the poorly immunogenic B16F10 model (Figure 3Q). Taken together, our data strongly suggested that signaling through Y319 regulated CD226 surface expression in CD8$^+$ TILs and that increased CD226 expression improved anti-tumor immunity and the efficacy of cancer immunotherapies.

CD226 is an important molecule for the IS and our scRNA-seq data showed that CD226$^{hi}$ T cells expressed a multitude of genes associated with the IS. While CD226 signaling through S329 has been shown to be important for IS formation in human CD4$^+$ T cells, little is known about the relevance of Y319. Thus, we assessed the quality of the IS between antigen-specific CD8$^+$ T cells and bone marrow-derived dendritic cells (BMDCs) by flow microscopy. We incubated WT., *Cd226*$^{Y319F}$., or *Cd226*$^{-/-}$.*Pmel-1* T cells with hgp100$_{25\text{-}33}$ peptide-pulsed BMDCs and measured the intensity of LFA-1 and F-actin at the interface of T cell-BMDC doublets (Figure S4K). *Cd226*$^{-/-}$.*Pmel-1* T cells showed impaired synapse quality, whereas the synapse quality of *Cd226*$^{Y319F}$.*Pmel-1* T cells was similar to WT.*Pmel-1* T cells (Figures S4L and S4M). This finding suggested that loss of CD226 surface expression but not the Y319 phosphorylation site reduced the ability of T cells to form high-quality IS. In turn, increased CD226 surface expression might improve the IS properties of *Cd226*$^{Y319F}$ T cells and partially explain their superior effector function.

## CD155-Induced Internalization of CD226 Depends on Phosphorylation of Y319 by Src Kinases

Given that CD155 is highly expressed in tumors, the frequency of CD226$^{neg}$ T cells correlate with tumor weight (Figures S5A and S5B), and *Cd155*$^{-/-}$ mice have elevated CD226 expression levels (Li et al., 2018; Seth et al., 2011), we hypothesized that tumor cell-derived CD155 contributed to loss of CD226 surface expression. To test this, we injected CD155-expressing (B16F10$^{ctrl}$) or -deficient (B16F10$^{Cd155-/-}$) B16F10 melanoma cells into either WT or *Cd155*$^{-/-}$ mice (Li et al., 2018) (Figure 4A). The frequency of CD226$^{neg}$ T cells infiltrating B16F10$^{Cd155-/-}$ melanoma was reduced in both WT and *Cd155*$^{-/-}$ mice compared to B16F10$^{ctrl}$ melanoma (Figure 4A). In concert, we observed higher frequencies of CD226$^{hi}$ T cells in WT and *Cd155*$^{-/-}$ mice bearing B16F10$^{Cd155-/-}$ melanoma (Figure S5C), supporting the idea that tumor cell-derived CD155 indeed contributes to loss of CD226 in T cells.

Next, we injected B16F10$^{ctrl}$ or B16F10$^{Cd155-/-}$ melanoma cells into WT or *Cd226*$^{Y319F}$ mice (Figure 4B). Consistent with our findings, we observed reduced frequencies of CD226$^{neg}$ T cells and increased frequencies of CD226$^{hi}$ T cells infiltrating B16F10$^{ctrl}$ tumors in *Cd226*$^{Y319F}$ compared to WT mice (Figures 4B and S5D). The frequencies of CD226$^{neg}$ T cells infiltrating B16F10$^{Cd155-/-}$ tumors in *Cd226*$^{Y319F}$ and WT mice were similar (Figures 4B and S5D), suggesting that CD155-induced loss of CD226 was indeed dependent on Y319. We still found CD226$^{neg}$ T cells infiltrating B16F10$^{Cd155-/-}$ tumors; thus, additional mechanisms appear to contribute to loss of CD226.

Next, we established an *in vitro* assay to study the underlying mechanism of CD155-induced loss of CD226 in CD8$^+$ T cells. Incubation of naive splenic CD8$^+$ T cells with CD3/CD28/CD155-coated beads (stim+CD155) led to profound loss of CD226 surface expression compared to CD3/CD28-coated beads (stim) (Figures 4C and S5E). T cells isolated from *Cd226*$^{Y319F}$ mice were largely resistant to CD155-induced loss of CD226 *in vitro* (Figure 4D). Notably, NK cells also lost CD226 surface expression upon ligation with CD155, which was partially dependent on the presence of Y319 (Figures S5F and S5G). Src kinases phosphorylate Y319 (Zhang et al., 2015), and using the specific Src kinase inhibitor PP2, we showed that phosphorylation of CD226 was required for CD155-mediated loss in both CD8$^+$ T cells and NK cells (Figure 4E, S5H, and S5I). Next, we

(F) Cytoplasmatic amino acid sequence of mCD226 showing the binding motifs for AP2 and CBL-B.
(G) Quantification of CD226$^{neg}$ splenic CD8$^+$ T cells treated as indicated (n = 3 spleens, mean ± SD, representative of two experiments).
(H) IC$_{50}$ values of peptides against a competitor peptide (mean ± SD, cumulative of three experiments).
(I) Histograms showing CD226 expression in CD8$^+$ T cells from WT or *Cbl-b*$^{\Delta R}$ mice (left) and corresponding quantification (right, n = 4 spleens, mean ± SD, representative of two experiments).
(J) Immunoblots showing Ubiquitin in CD8$^+$ T cells stimulated with CD3+CD28 ± CD155 in presence of MG132 for 180 min before (left, 10% of total protein, "INPUT") and after immunoprecipitation of CD226 (right, "IP: α-CD226"); loading control: β-actin.
(K–N) Representative immunoblots showing CD226 in CD8$^+$ T cells isolated from WT mice (K), WT and *Cd226*$^{Y319F}$ mice (L), *Cbl-b*$^{\Delta R}$ mice (M) stimulated with CD3+CD28 ± CD155, and WT mice (N) stimulated with CD3+CD28 ± CD155 in presence of MG132; loading control: β-actin (representative of 2–4 experiments).
Statistics: one-way ANOVA with post hoc Tukey's for multiple comparisons (A, B, D, E, G, and I); *p < 0.05, **p < 0.01, ***p < 0.001, ****p < 0.0001.

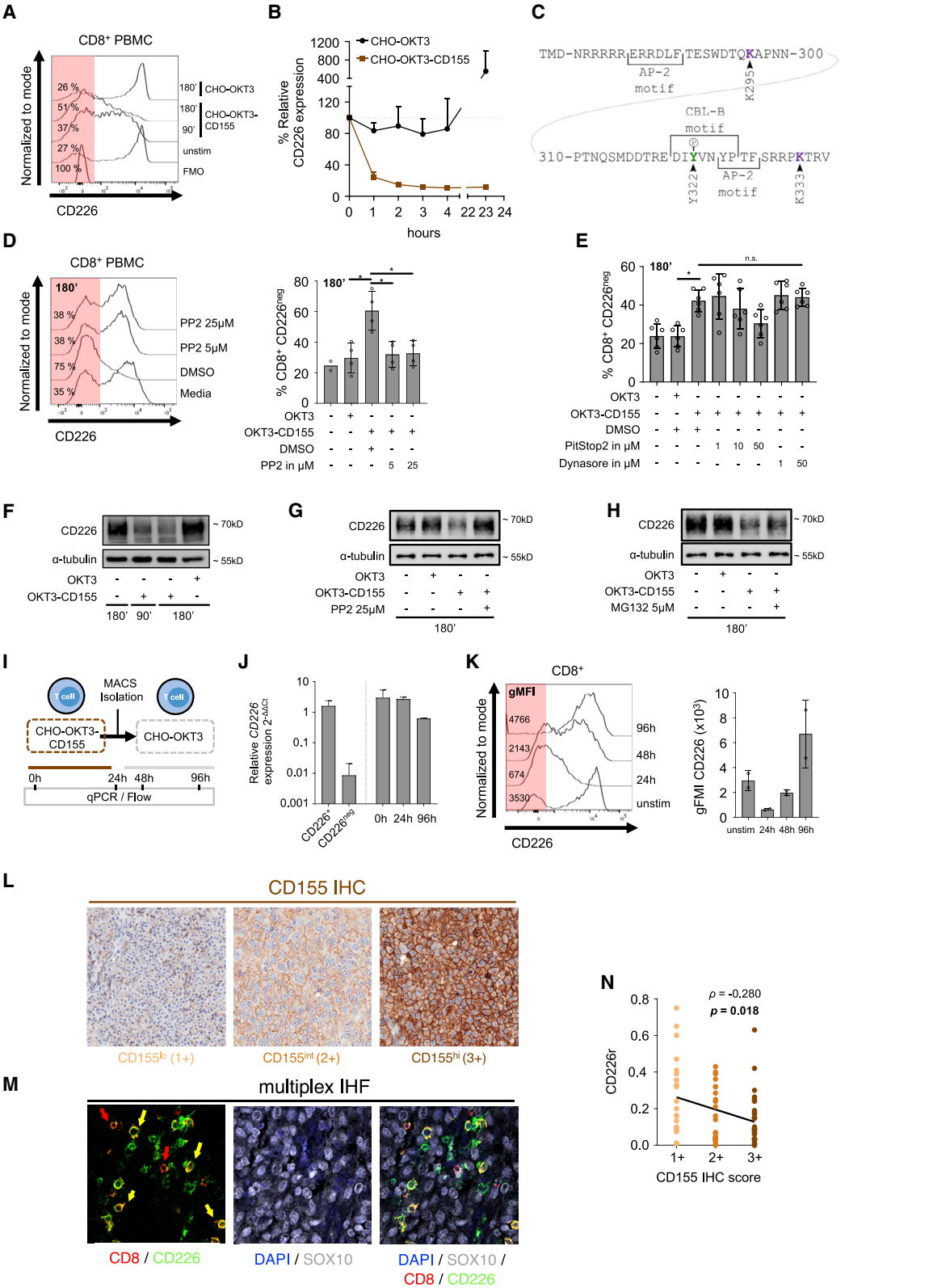


*(legend on next page)*

quantified surface and intracellular CD226 expression in WT or *Cd226*$^{Y319F}$ T cells incubated with CD155 or control. CD155 ligation increased the MFI of intracellular CD226 compared to control (Figure S5J), supporting the idea of CD155-induced internalization of CD226.

### Post-transcriptional Regulation of CD226 Depends on Ubiquitination via Cbl-b and Proteasomal Degradation

In T cells, AP2-dependent clathrin-mediated endocytosis (CME) contributes to the post-transcriptional regulation of immune receptors including CTLA-4 and CD3 (Shiratori et al., 1997; Manrique et al., 2017). The cytoplasmic tail of CD226 contains an AP2 binding motif **Y**xx**Θ** (Θ represents a large hydrophobic residue) starting at Y322 (**Y**PT**F**) (Figure 4F). Inhibition of CME using the small molecule inhibitors PitStop2 and Dynasore did not impair CD155-induced loss of CD226 (Figures 4G and S5K). Notably, the cytoplasmic tail of CD226 also possesses a tyrosine kinase-binding (TKB) motif **D**x(**pY**) xxxP, starting at D317 (**D**G**Y**$_{319}$VNYP) and including **Y**319, which after phosphorylation might enable the binding of the E3 ubiquitin ligase Cbl-b (Figure 4F). In fact, ubiquitination represents a critical pathway of post-transcriptional regulation in T cells (O'Leary et al., 2015). Surface plasmon resonance (SPR) experiments showed that CD226 peptides phosphorylated at Y319, but not Y319F mutant peptides, bound to the purified TKB domain from Cbl-b, with a similar $IC_{50}$ to peptides from a well-known Cbl-b target IRS-1 (cblin) (Figures 4H and S5L). To determine the contribution of Cbl-b E3 ubiquitin ligase activity for the regulation of CD226, we isolated CD8$^+$ T cells from *Cbl-b*$^{C373A}$ mice (further referred to as *Cbl-b*$^{\Delta R}$), which harbor a loss-of-function mutation in the RING finger domain abrogating the E3 ubiquitin-ligase function (Oksvold et al., 2008). T cells from *Cbl-b*$^{\Delta R}$ mice were also resistant to CD155-induced loss of CD226 surface expression (Figure 4I). Immunoprecipitation of CD226 further showed ubiquitination of CD226 upon activation and CD155 ligation (Figure 4J). Immunoblot analysis demonstrated that CD155 ligation reduced CD226 protein levels, suggesting that CD226 was degraded upon internalization (Figure 4K). T cells isolated from *Cd226*$^{Y319F}$ or *Cbl-b*$^{\Delta R}$ mice were both resistant to CD155-induced CD226 degradation (Figures 4L and 4M), and experiments using the proteasome inhibitor MG-132 revealed that degradation of CD226 was partially dependent on the proteasome (Figure 4N).

### CD155 Induces Post-transcriptional Regulation of CD226 in Human CD8$^+$ T Cells

Consistent with the dynamic regulation of CD226 in mouse T cells, human CD8$^+$ T cells also increased CD226 surface expression upon TCR activation (Figure S6A). To assess the impact of CD155 on CD226 surface expression in human CD8$^+$ T cells, we used CHO cells stably expressing OKT3 alone (CHO-OKT3) or in combination with high levels of CD155 (CHO-OKT3-CD155) (Figure S6B). CD8$^+$ T cells isolated from PBMCs of healthy donors (HDs) co-cultured with CHO-OKT3-CD155 cells showed substantially reduced CD226 surface expression within a few hours, while CD226 surface expression was increased 24 h after co-culture with CHO-OKT3 cells (Figures 5A and 5B). We also demonstrated a CD155 dose-dependent loss of CD226 in our co-culture assays either using CHO cells expressing various levels of CD155 or by using increasing amounts of CD155 blocking antibodies (Figures S6C and S6D).

The cytoplasmic tail of human CD226 has a CBL-B binding motif starting at D320 (DIYVNYP) and a tyrosine-based internalization motif for AP2 starting at Y325 (YPTF). In addition, human CD226 contains a potential dileucine-based internalization motif (**E**xxx**LΘ**) starting at E282 (**E**RRD**LF**), for the interaction with AP2 (Figure 5C). Consistent with our findings in mouse T cells, Src kinase inhibition impaired CD155-induced loss of CD226 (Figure 5D), while inhibition of AP2-dependent CME did not reduce the frequency of CD226$^{neg}$ T cells upon co-culture with CHO-OKT3-CD155 cells (Figure 5E). SPR analysis demonstrated that only CD226 peptides phosphorylated at Y322, the homolog to mouse Y319, were able to bind the purified TKB domain of CBL-B (Figure S6E), suggesting that CD226 expression in human T cells was also regulated through CBL-B. Human CD226 has two cytoplasmic lysine residues K295 and K333, which could be ubiquitinated by CBL-B (Figure 5C). We transduced Jurkat T cells with either WT *CD226* (*CD226*$^{WT}$) or a variant that lacked both cytosolic lysine residues (*CD226*$^{K295A+K333A}$). We

**Figure 5. CD155 Induces Ubiquitination and Proteasomal Degradation of CD226 in Human CD8$^+$ T Cells**

(A) Histograms showing CD226 expression in CD8$^+$T cells from HD PBMCs after co-culture with CHO-OKT3 or CHO-OKT3-CD155.

(B) Quantification of CD226 expression (mean ± SD, n = 3 HD).

(C) Cytoplasmatic amino acid sequence of hCD226 showing the binding motifs for AP2 and CBL-B (TMD, transmembrane domain).

(D) Histograms showing CD226 expression in CD8$^+$T cells from HD PBMCs treated as indicated (left) and corresponding quantification (right, cumulative of n = 2–4 HD, mean ± SD).

(E) Flow cytometric quantification of CD226$^{neg}$CD8$^+$ T cells treated as indicated (right, cumulative of n = 6 HD, mean ± SD).

(F–H) Immunoblot images showing CD226 protein level in CD8$^+$T cells from HD PBMC co-cultured as indicated (F), in the presence of the src-inhibitor PP2 (G), or the proteasome-inhibitor MG132 (H); loading control: α-Tubulin (representative of two experiments).

(I) Experimental setup.

(J) Relative *CD226* expression normalized to *GAPDH* for indicated samples (n = 2 HD PBMCs, mean ± SD).

(K) Representative histograms showing CD226 expression on CD8$^+$T cells in HD PBMCs (left) and corresponding quantification of CD226 gMFI (right, mean ± SD, n = 2 HD, representative of two experiments).

(L–N) Correlation of CD155 expression and infiltration of CD226$^+$CD8$^+$/CD8$^+$ (CD226r) T cells.

(L) Representative CD155-IHC images showing low CD155 expression (left, score 1+), intermediate (middle, score 2+), and high CD155 expression (right, score 3+).

(M) Representative mIHF images of melanoma samples. Yellow arrows indicate co-localization of CD226 and CD8.

(N) Correlation of CD226r with CD155 score in melanoma samples (n = 74).

Statistics: RM one-way ANOVA with post hoc Tukey's for multiple comparisons (D and E), Spearman rank correlation coefficient "ρ" (N); *p < 0.05, **p < 0.01.

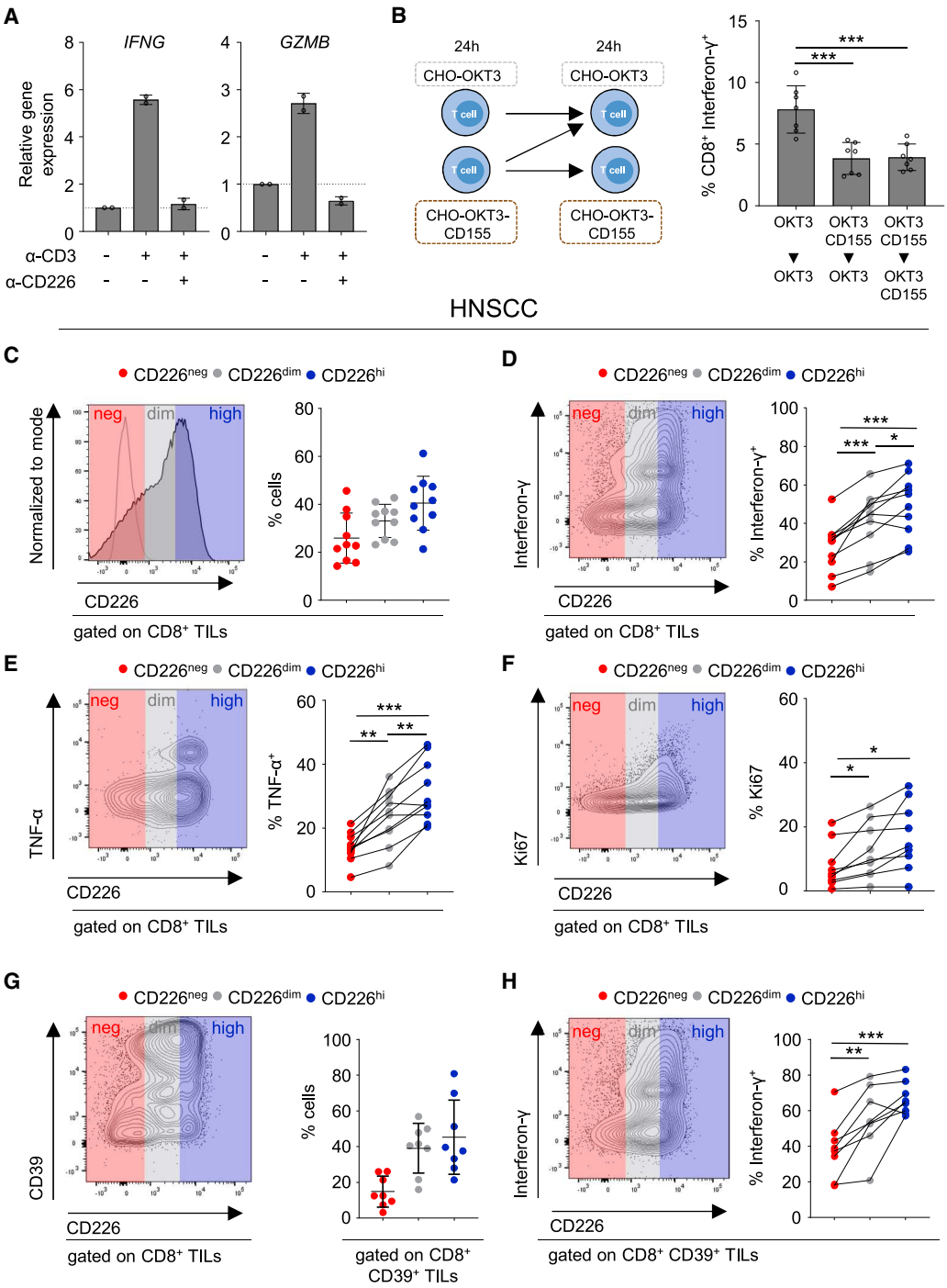


**Figure 6. CD226 Correlates with Effector Function in Tumor-Infiltrating T Cells in HNSCC Patients**

(A) Relative expression of *IFNG* and *GZMB* in PBMCs after indicated stimulation for 48 h (n = 2 HD).

(B) Experimental setup (left) and flow cytometric quantification of IFNγ$^+$CD8$^+$ T cells (right, cumulative of n = 7 HD, mean ± SD).

(C) Histogram showing CD226 expression on CD8$^+$ HNSCC TILs (left) and corresponding quantification (right, n = 10, mean ± SD).

(D–F) Contour plots showing CD226 and IFNγ (D), TNFα (E), and Ki67 (F) in CD8$^+$ TILs (left) and quantification across CD226 subsets (right; n = 9–10).

(G and H) Representative contour plot showing CD226 and CD39 in CD8$^+$ TILs (left) (G) and corresponding quantification of IFNγ in CD8$^+$CD39$^+$TILs (H) (right; n = 8, mean ± SD).

Statistics: one-way ANOVA with post hoc Tukey's for multiple comparisons (B), RM one-way ANOVA with post hoc Tukey's for multiple comparisons (D, E, F, and H); *p < 0.05, **p < 0.01, ***p < 0.001.

found that genetic deletion of both lysine residues rendered *CD226*$^{K295A+K333A}$ Jurkat cells largely resistant to CD155-induced loss of CD226 (Figure S6F). Immunoblot analysis further showed that total CD226 protein levels were reduced upon CD155 ligation (Figure 5F) and phosphorylation of Y322 by Src kinases (Figure 5G). Consistent with our findings in mouse T cells, inhibition of the proteasome using MG-132 partially blocked CD226 degradation upon CD155 ligation (Figure 5H).

Next, we assessed whether CD155 ligation also influenced the transcriptional regulation of CD226. Here, we generated CD226$^{neg}$ T cells by co-culture with CHO-OKT3-CD155 cells for 24 h. Subsequently, CD226$^{neg}$ T cells were purified and co-cultured with CHO-OKT3 cells for 24 or 72 h to assess both CD226 surface and mRNA expression (Figure 5I). In contrast to mice, we found a variable, but proportion of CD226$^{neg}$ T cells in the blood of HD with little to no *CD226* mRNA expression compared to CD226$^{+}$ cells (Figure 5J). While the majority of T cells lost CD226 surface expression after co-culture with CHO-OKT3-CD155 cells (Figure 5K), we still detected *CD226* mRNA at comparable levels to resting T cells (Figure 5J). Interestingly, 72 h after the withdrawal of CD155, human CD8$^{+}$ T cells regained CD226 surface expression, suggesting that CD155-induced loss of CD226 was reversible and not detectably regulated at the transcriptional level (Figures 5J and 5K).

To assess if high levels of CD155 influence CD226 surface expression in T cells in the TME of cancer patients, we determined tumor cell CD155 expression and the number of CD226$^{+}$ cells in CD8$^{+}$ T cells (CD226r) in melanoma patient specimens by immunohistochemistry (IHC) and multiplex immunohistofluorescence (mIHF), respectively. As previously described (Lepletier et al., 2020), intra-tumor membrane staining for CD155 was very homogeneous, but inter-patient variability existed. Briefly, 28% (21/74) of melanoma specimens showed low CD155 expression (score 1+), 32% (24/74) showed intermediate (score 2+), and 40% (30/74) showed strong CD155 staining (score 3+) (Figure 5L). Indeed, mIHF analyses showed that a high CD226r was inversely correlated with CD155 protein expression in melanoma samples (Figures 5M and 5N). In addition, we found a slight inverse correlation between *CD226* and *PVR* (CD155) but not *NECTIN2* (CD112) gene expression in the TCGA dataset (Figure S6G).

## CD226 Expression Correlates with Effector Function in Human TILs

Gene expression analysis of PBMCs activated in the presence or absence of CD226-blocking antibodies showed that TCR-induced *IFNG* and *GZMB* expression was dependent on CD226 (Figure 6A). Given that CD155 ligation induced profound loss of CD226, we next measured IFN$\gamma$ production in restimulated T cells, which have been previously co-cultured with CHO-OKT3 or CHO-OKT3-CD155 cells for 24 h (Figure 6B). We found higher frequencies of IFN$\gamma^{+}$ T cells co-cultured and restimulated with CHO-OKT3 compared to T cells pre-activated in the presence of CD155 (Figure 6B). Next, we assessed CD226 expression in CD8$^{+}$ T cells isolated from fresh tumor samples from head and neck squamous cell carcinoma (HNSCC) patients. As in mice, human CD8$^{+}$ TILs showed variable surface expression of CD226 (Figure 6C). Flow cytometric analysis of *ex vivo* stimulated CD8$^{+}$ HNSCC TILs showed a correlation between CD226 surface expression and T cell fitness as evidenced by increased IFN$\gamma$, TNF$\alpha$, Ki67, and CD107a staining (Figures 6D–6F and S7A). TCGA analysis further showed that *CD226* gene expression was associated with improved survival in HNSCC patients and correlated with *CD8B*, *IFNG*, and *GZMB* but not with *NCAM1* (CD56) expression, a classical NK cell marker (Figures S7B and S7C). Similar to in mice, only a small fraction of CD8$^{+}$CD39$^{+}$ or CD8$^{+}$PD-1$^{+}$ HNSCC TILs were negative for CD226, and the frequency of IFN$\gamma^{+}$ cells within CD8$^{+}$CD39$^{+}$ and CD8$^{+}$PD-1$^{+}$ HNSCC TILs correlated with CD226 surface expression (Figures 6G, 6H, and S7D).

## CD226 Surface Expression in CD8$^{+}$ TILs Correlate with Response to ICB in Melanoma

Next, we asked whether the response to ICB in melanoma patients correlated with the presence of CD226$^{+}$CD8$^{+}$ TILs. We determined the frequency of tumor-infiltrating CD226$^{+}$ cells in CD8$^{+}$ T cells (CD226r) by mIHF in pre-ICB treatment samples from a discovery cohort including 31 melanoma patients (Sydney; Figure 7A, Table S1). Indeed, a high CD226r was associated with improved progression-free survival (PFS, HR 3.38; p = 0.036; Figure 7B). Notably, the survival benefit associated with high CD226r was independent of total numbers of CD8$^{+}$ T cells present (HR 2.15; p = 0.163; Figure 7C). To substantiate our findings, we determined CD226r in a validation cohort including 43 patients from two clinical centers (St. Gallen and Bonn; Table S1). In our validation, cohort patients with a high CD226r also displayed a prolonged PFS (HR 2.95; p = 0.002; Figure 7D). Again, the observed survival benefit was independent of high infiltration with CD8$^{+}$ T cells (HR 1.87; p = 0.091; Figure 7E). Of note, a high CD226r was associated with an improved PFS in both the St. Gallen cohort (n = 19; HR 4.20; p = 0.033; Figure S7F) and the Bonn cohort (n = 24; HR 4.67; p = 0.020; Figure S7G). We also noticed a prolonged PFS for patients with low expression of CD155 (Figure S7H). Stratification of patients based on CD226r and CD155 expression resulted in increased predictive power for PFS (HR 4.352; p = 0.001; Figure S7H). Thus, staining for CD226 might allow us to identify highly functional CD8$^{+}$ T cells with in the TME and potentially improve the prediction of response to ICB. Overall, we demonstrated in mice and human samples that CD155-induced internalization and degradation of CD226 represents a resistance mechanism used by tumors to escape anti-tumor immunity.

## DISCUSSION

Current research focuses on understanding the importance of inhibitory receptors expressed on tumor-infiltrating T cells. In contrast, our knowledge of the function and regulation of activating T cell receptors in cancer is limited. CD226 is an activating receptor important for NK and T cell function. Although, CD226 has an established role in anti-tumor immunity (Gilfillan et al., 2008; Iguchi-Manaka et al., 2008), the underlying mechanisms remain unclear. Here, we discovered a mechanism of immune escape in which tumor cells disarm cytotoxic T cells through CD155-mediated internalization and degradation of the activating receptor CD226. Further understanding of this resistance mechanism might help to predict patient responses to ICB and potentially the development of novel immunotherapies that

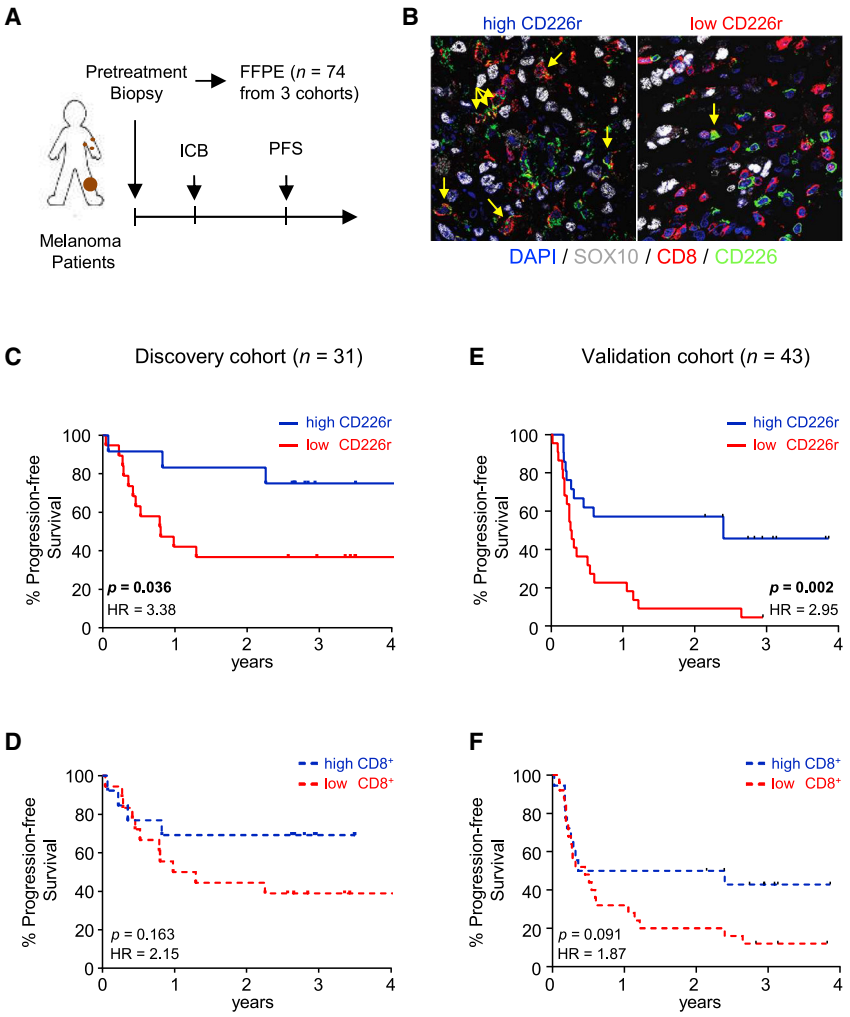


**Figure 7. CD226 Expression in CD8⁺ T Cells Correlates with Prolonged Progression-free Survival Following ICB Therapy in Melanoma Patients**

(A) Experimental setup.

(B) Representative mIHF images of human melanoma samples with high and low CD226r. Yellow arrows indicate co-localization of CD226 and CD8.

(C–F) Kaplan-Meier survival curves showing PFS in patients from indicated cohorts stratified by high and low CD226r (C and D) or high and low counts of CD8⁺ T cells (E and F). (Discovery cohort n = 31, validation cohort n = 43).

Statistics: log-rank (Mantel-Cox) test.

maintain or enhance CD226 expression on tumor infiltrating CD8⁺ T cells.

Co-expression of inhibitory receptors, e.g., CD39, PD-1, and Tim-3, alongside transcription factors such as EOMES and TOX are used to identify dysfunctional or exhausted T cells (Bengsch et al., 2018; Khan et al., 2019; Scott et al., 2019; Wang et al., 2019; Wherry and Kurachi, 2015). However, most of these molecules are also induced upon T cell activation, introducing difficulties in the identification of highly functional versus dysfunctional TILs. We showed that IFNγ production correlated with the presence of CD226 even in T cells that expressed multiple inhibitory receptors. Our findings are supported by a recent study showing that *Cd226* gene expression in tumor-infiltrating CD8⁺ T cells is highly associated with activation but only weakly with exhaustion (Singer et al., 2016). Here, we propose that loss of CD226 represents a complementary mechanism of T cell dysfunction and that CD226 expression in conjunction with inhibitory receptors could serve as a marker to discriminate functional and dysfunctional T cells in cancer.

Besides its function as an activating receptor, CD226 is an adhesion molecule, interacts with the cytoskeleton (Ralston et al., 2004), and plays an important role for the formation of the IS (Dustin, 2014, Díaz et al., 2018). Using scRNA-seq we found a large number of genes associated with cell adhesion and IS formation enriched in CD226$^{hi}$ compared to CD226$^{neg}$ T cells, including CD11a and CD18, which form LFA-1, a key component of the IS. Weulersse et al. (2020) showed that the conversion of LFA-1 into its high-affinity form requires surface expression of CD226. The co-localization of CD226 with LFA-1, and also the recruitment of the LFA-1/CD226 complex toward the IS in T cells, is dependent on phosphorylation of serine 326 (S326) (Shibuya et al., 1999; Shirakawa et al., 2005; 2006). In concert with these findings, we confirmed that genetic deletion of *Cd226* reduced the synapse quality, whereas the mutation Y319F did not affect synapse quality *in vitro*. Since CD226 is important for the amplification of TCR signaling independent of the IS (Weulersse et al., 2020; Gaud et al., 2018), both mechanisms could explain the superior anti-tumor immunity observed in *Cd226*$^{Y319F}$ mice. Future studies will need to further dissect the relevance and function of other signaling components of CD226 in CD8⁺ T cells for anti-tumor immunity.

CD226 (together with CD27 and CD28) belongs to a limited number of activating receptors that are constitutively expressed on T cells (Chen and Flies, 2013). However, there are fundamental differences in the expression of ligands for those receptors: while CD70 (ligand of CD27) and CD80/CD86 (ligands for CD28) are predominantly expressed within lymphoid structures, the ligand for CD226, CD155, is highly expressed on mouse and human tumor cells (Bottino et al., 2003; Li et al., 2018). Using *in vitro* and *in vivo* systems, we showed that CD155 post-transcriptionally regulated CD226 surface expression in mouse and human T cells. We discovered that after CD155 ligation, the phosphorylation of Y319 in mouse or Y322 in human T cells through Src kinases enabled binding of the E3 ubiquitin ligase CBL-B, ubiquitination, internalization, and proteasomal degradation of CD226. The importance of CBL-B for T cell activation and function in cancer is well established (Chiang et al., 2007; Chiang et al., 2000; Loeser et al., 2007); however, how much of its effect can be attributed to the regulation of CD226 remains unknown. Additionally, other mechanisms beside ubiquitination

and proteasomal degradation might contribute to the regulation of CD226 surface expression and warrant further investigations.

Our scRNA-seq data and the findings that human CD226$^{neg}$ T cells isolated from the blood of HDs did not express *CD226* mRNA show that CD226 is also regulated at the transcriptional level. Indeed, the transcription factor *Eomes* was enriched in CD226$^{neg}$ T cells, which was consistent with the work from Weulersse et al. (2020), who provided evidence that Eomes contributes to the transcriptional regulation of *Cd226*. When characterizing the differences between T cell subpopulations, CD226$^{hi}$ T cells showed increased expression of the transcription factors RAR-related orphan receptor $\alpha$ (*Rora*) and *Id2*. Although little is known about the role of *Rora* in CD8$^+$ T cells, some reports suggest that *Rora* is associated with T cell activation and memory formation (Billingsley et al., 2015; He et al., 2016). Transcriptional analysis of CD8$^+$ T cells in a LM-OVA model identified *Rora* as a regulator of CD8$^+$ effector T cells (Best et al., 2013). Thus, future work needs to investigate the impact of prolonged CD226 expression for T cell differentiation and memory formation. In CD226$^{neg}$ T cells, we observed increased expression of the activating receptors *Crtam*, *Tnfrsf4* (OX40), and *Tnfrsf9* (CD137). These genes were recently found to be associated with an exhaustion phenotype in tumor-infiltrating T cells and to a lesser extent in LCMV-specific T cells (Mognol et al., 2017). Overall, T cell subsets classified by CD226 expression seem to rely on different transcriptional programs that are associated with effector function in CD226$^{hi}$ and dysfunction in CD226$^{neg}$ T cells.

Using *Cd226*$^{-/-}$ mice or CD226-blocking antibodies, we and Weulersse et al. (2020) showed that multiple cancer immunotherapies required the expression of CD226 in CD8$^+$ T cells. Accordingly, increased CD226 surface expression improved the efficacy of ICB and ACT in mice. In concert with our findings, Wang et al. (2018) recently found that the efficacy of anti-PD1 and anti-GITR antibodies was also dependent on CD226. The importance of CD226 for cancer immunotherapy was also evidenced during our review process by Jin et al. (2020) in the context of anti-TIGIT mAb treatment. Using pre-ICB treatment samples from melanoma patients, we showed that infiltration with CD226$^+$CD8$^+$ T cells correlated with prolonged PFS. Although ICB has revolutionized the treatment of cancer, we have not yet identified robust biomarkers that stratify patients as CD8$^+$ T cell infiltration, PD-L1 expression, or tumor mutational burden are not conclusive. Our work provides evidence that CD226 marks highly functional T cells required for the efficacy of ICB in melanoma patients. In summary, we and Weulersse et al. (2020) postulate that CD226 expression is an important rheostat for the fitness of tumor-infiltrating CD8$^+$ T cells and that loss of CD226 contributes to resistance to cancer immunotherapy.

### Limitations of Study

Here, we showed that tumor cells impair T cell fitness through CD155-mediated degradation of the activating receptor CD226. While we discovered that phosphorylation of Y319 is important for ubiquitination and proteasomal degradation of CD226, further studies will need to assess whether other mechanisms (e.g., lysosomal degradation) contribute to the regulation of CD226 surface expression.

We also showed that a mutation in Y319 led to increased CD226 expression and superior tumor immunity. However, the underlying mechanism remains elusive. Further studies will need to test the impact of the CD226 Y319 mutation on T cell receptor signaling, activation, function, as well as memory formation. Additionally, future studies will need to assess how other signaling domains, e.g., S326, affect T cell fitness and cancer immunotherapy.

Although clinically a high ratio of CD226$^+$CD8$^+$ T cells correlated with PFS in patients treated with ICB, subsequent studies will need to confirm the relevance of CD226 for the efficacy of ICB in larger patient cohorts and other cancer types beyond melanoma.

## STAR★METHODS

Detailed methods are provided in the online version of this paper and include the following:

- KEY RESOURCES TABLE
- RESOURCE AVAILABILITY
  - Lead Contact
  - Materials Availability
  - Data and code Availability
- EXPERIMENTAL MODEL AND SUBJECT DETAILS
  - Mice
  - Cell lines
  - Primary cell cultures
  - Patients and healthy donor specimens
  - Validation cohort
- METHOD DETAILS
  - In Vivo tumor models
  - Tissue processing
  - Flow cytometry
  - Cytokine Bead Array
  - Generation of CRISPitope-engineered cell line (HCmel12$^{hgp100}$)
  - Transduction of mouse CD8$^+$ T cells
  - T cell stimulation assays
  - NK cell stimulation assays
  - CD226 internalisation assay
  - Analyses of immunological synapse formation
  - Transduction of Jurkat cells
  - Human T cell bead-stimulation assays
  - Generation of OKT3+/− CD155 expressing CHO cells
  - hCD226-CD155 interaction using artificial APC
  - Immunoblot
  - Immunoprecipitation of CD226
  - CBL-B TKB-Protein production
  - Surface Plasmon Resonance (SPR)
  - qPCR analysis
  - Gene expression analysis of human PBMCs
  - Generation and sequencing of single cell libraries
  - NGS data analysis
  - Immunohistochemical staining for human CD155
  - Multiplex immunohistofluorescence (mIHF) staining
  - Multiplex-IHF Image acquisition and analysis
  - The Cancer Genome Atlas (TCGA) transcriptomic analysis
  - Moving average analysis
  - Survival analysis of TCGA transcriptomic data
- QUANTIFICATION AND STATISTICAL ANALYSIS

## SUPPLEMENTAL INFORMATION

Supplemental Information can be found online at https://doi.org/10.1016/j.immuni.2020.09.010.

## ACKNOWLEDGMENTS

We would like to thank L. Town, A. Zaharia, K. Elder, P. Collins, M. Flynn, and S. Ng as well as the Core facilities at QIMR Berghofer for excellent technical assistance. We are grateful to Dr W.Y. Langdon from the University of Western Australia for providing the Cbl-b mutant mouse. The project was supported by the BioBank Core Facility of the University Hospital Bonn, Germany. M.B. is supported by a scholarship of the Dr. Mildred Scheel Stiftung fuer Krebsforschung of the Deutsche Krebshilfe. T.B. was supported by a NHMRC Early Career Research Fellowship (1138757) and project grant (1124690) and a Melanoma Research Alliance Young Investigator grant (693786). M.J.S. was supported by a NHMRC Investigator Award (1173958) and program grant (1132519). M.J.S. and I.D. were supported by a Cancer Council Queensland project grant (1157048). A.V. is supported by grants from the Canadian Institutes of Health Research (MT-14429, MOP-82906, FDN-143338) and holds the Canada Research Chair on Signaling in the Immune System. M.H. was supported by the Deutsche Forschungsgemeinschaft (DFG, German Research Foundation) within GRK 2168. M.E. was supported by a scholarship within GRK 2168. M.H. and M.G. are funded by the DFG under Germany's Excellence Strategy (EXC2151-390873048). J.S.W. is supported by a NHMRC fellowship, the Melanoma Institute Australia, the New South Wales Ministry of Health, NSW Health Pathology, Cancer Institute NSW, and the Ainsworth Foundation. R.A.S and G.V.L. are supported by NHMRC Practitioner Fellowship. G.V.L. is supported by the University of Sydney Medical Foundation and Melanoma Institute Australia. This work was funded by the National Breast Cancer Foundation Australia (IIRS-18-159) and NHMRC (APP1185907) to A.M. O.T.P. is supported by a grant from the Cancer Research Center of the University Hospital and the University of Zurich. L.F. is supported by a grant from the Swiss National Science Foundation (PP00P3_157448).

## AUTHORS CONTRIBUTION

Conceptualization, M.B., W.C.D., R.J.J., L.M., M.J.S., and T.B.; Methodology, M.B., A.R.A., D.C., L.G.L., R.L., L.T.K., A.L., J.M., E.Y.S., S.E.N., A.M., R.J.J., and T.B.; Investigation: M.B., A.S., A.R.A., D.C., K.S., S.K., I.D., L.G.L., L.G.M.G., K.L., R.L., N.S., M.V.J., S.H., G. Kelly, F.V., A.L., A.R., B.Q., M.C., K.N., E.Y.S., O.T.P., A.V., M.J.S., and T.B.; Resources, S.P., S.J., M.E., M.H., M.G., G. Kristiansen, T.T., E.A., B.G.M.H., J.S.W., G.V.L., R.A.S., M.D.B., J.L., D.D., L.F., A.V., S.E.N., and A.M.; Writing, M.B., L.M., M.J.S., and T.B.; Supervision, M.J.S. and T.B.; Funding Acquisition, M.B., M.J.S., and T.B.

## DECLARATION OF INTERESTS

M.J.S. has research agreements with Bristol Myers Squibb (BMS) and Tizona Therapeutics and is on the Scientific Advisory Board of Tizona Therapeutics and Compass Therapeutics. T.B. has research agreements with BMS. B.G.M.H. is a consultant advisor to BMS, Merck Sharp and Dohme, Roche, AstraZenca, Pfizer, Eisai, and Takeda and has research agreements with Amgen. G.V.L. is a consultant advisor to Aduro, Amgen, Mass-Array, BMS, Merck MSD, Novartis, Roche, OncoSec Medical, Sandoz, and Pierre Fabre. A.M. is a consultant advisor for BMS, Merck MSD, Novartis, Roche, and Pierre Fabre. W.C.D. declares a scientific research agreement with BMS, consulting agreements with Omeros Corp. and Cascadia Drug Development Group, and receipt of speaker's honoraria from Amgen. A.V. has research agreements with BMS. R.A.S. has received fees for professional services from Novartis Pharma AG, MSD Sharp & Dohme (Australia), NeraCare, AMGEN Inc., BMS, Novartis Pharmaceuticals Australia Pty. Limited, Myriad Genetics GmbH, GlaxoSmithKline Australia. L.F. reported grants from the Swiss National Science Foundation, Swiss Cancer League, Hookipa Pharma, Krebsliga Schweiz, and Novartis Foundation as well as an advisory role for Novartis and BMS. S.E.N. has a research agreement with Servier. M.B., M.J.S., and T.B. have registered a patent for the use of CD226 in cancer immunotherapies (Australian Provisional Patent Application No. 2019900621).

Received: September 25, 2019
Revised: May 21, 2020
Accepted: September 15, 2020
Published: October 13, 2020

## REFERENCES

Ardolino, M., Zingoni, A., Cerboni, C., Cecere, F., Soriani, A., Iannitto, M.L., and Santoni, A. (2011). DNAM-1 ligand expression on Ag-stimulated T lymphocytes is mediated by ROS-dependent activation of DNA-damage response: relevance for NK-T cell interaction. Blood *117*, 4778–4786.

Ashhurst, T.M. (2017). tSNEplots R script. (Github).

Attanasio, J., and Wherry, E.J. (2016). Costimulatory and Coinhibitory Receptor Pathways in Infectious Disease. Immunity *44*, 1052–1068.

Auguie, A. (2017). gridExtra: Miscellaneous Functions for "Grid" Graphics. R package version 2.3. (R Project for Statistical Computing).

Bald, T., Quast, T., Landsberg, J., Rogava, M., Glodde, N., Lopez-Ramos, D., Kohlmeyer, J., Riesenberg, S., van den Boorn-Konijnenberg, D., Hömig-Hölzel, C., et al. (2014). Ultraviolet-radiation-induced inflammation promotes angiotropism and metastasis in melanoma. Nature *507*, 109–113.

Bengsch, B., Ohtani, T., Khan, O., Setty, M., Manne, S., O'Brien, S., Gherardini, P.F., Herati, R.S., Huang, A.C., Chang, K.M., et al. (2018). Epigenomic-Guided Mass Cytometry Profiling Reveals Disease-Specific Features of Exhausted CD8 T Cells. Immunity *48*, 1029–1045.e5.

Best, J.A., Blair, D.A., Knell, J., Yang, E., Mayya, V., Doedens, A., Dustin, M.L., and Goldrath, A.W.; Immunological Genome Project Consortium (2013). Transcriptional insights into the CD8(+) T cell response to infection and memory T cell formation. Nat. Immunol. *14*, 404–412.

Billingsley, J.M., Rajakumar, P.A., Connole, M.A., Salisch, N.C., Adnan, S., Kuzmichev, Y.V., Hong, H.S., Reeves, R.K., Kang, H.J., Li, W., et al. (2015). Characterization of CD8+ T cell differentiation following SIVΔnef vaccination by transcription factor expression profiling. PLoS Pathog. *11*, e1004740.

Blake, S.J., Stannard, K., Liu, J., Allen, S., Yong, M.C., Mittal, D., Aguilera, A.R., Miles, J.J., Lutzky, V.P., de Andrade, L.F., et al. (2016). Suppression of Metastases Using a New Lymphocyte Checkpoint Target for Cancer Immunotherapy. Cancer Discov. *6*, 446–459.

Blighe, K., Rana, S., and Lewis, M. (2020). EnhancedVolcano: Publication-ready volcano plots with enhanced colouring and labeling. R package version 1.6.0. (Bioconductor).

Bottino, C., Castriconi, R., Pende, D., Rivera, P., Nanni, M., Carnemolla, B., Cantoni, C., Grassi, J., Marcenaro, S., Reymond, N., et al. (2003). Identification of PVR (CD155) and Nectin-2 (CD112) as cell surface ligands for the human DNAM-1 (CD226) activating molecule. J. Exp. Med. *198*, 557–567.

Budczies, J., Klauschen, F., Sinn, B.V., Győrffy, B., Schmitt, W.D., Darb-Esfahani, S., and Denkert, C. (2012). Cutoff Finder: a comprehensive and straightforward Web application enabling rapid biomarker cutoff optimization. PLoS ONE *7*, e51862.

Burns, G.F., Triglia, T., Werkmeister, J.A., Begley, C.G., and Boyd, A.W. (1985). TLiSA1, a human T lineage-specific activation antigen involved in the differentiation of cytotoxic T lymphocytes and anomalous killer cells from their precursors. J. Exp. Med. *161*, 1063–1078.

Canale, F.P., Ramello, M.C., Núñez, N., Araujo Furlan, C.L., Bossio, S.N., Gorosito Serrán, M., Tosello Boari, J., Del Castillo, A., Ledesma, M., Sedlik, C., et al. (2018). CD39 Expression Defines Cell Exhaustion in Tumor-Infiltrating CD8$^+$ T Cells. Cancer Res. *78*, 115–128.

Carlson, M. (2019). org.Mm.eg.db: Genome wide annotation for Mouse. R package version 3.8.2. (Bioconductor).

Chan, C.J., Martinet, L., Gilfillan, S., Souza-Fonseca-Guimaraes, F., Chow, M.T., Town, L., Ritchie, D.S., Colonna, M., Andrews, D.M., and Smyth, M.J. (2014). The receptors CD96 and CD226 oppose each other in the regulation of natural killer cell functions. Nat. Immunol. *15*, 431–438.

Chen, L., and Flies, D.B. (2013). Molecular mechanisms of T cell co-stimulation and co-inhibition. Nat. Rev. Immunol. *13*, 227–242.

Chiang, Y.J., Kole, H.K., Brown, K., Naramura, M., Fukuhara, S., Hu, R.J., Jang, I.K., Gutkind, J.S., Shevach, E., and Gu, H. (2000). Cbl-b regulates the CD28 dependence of T-cell activation. Nature *403*, 216–220.

Chiang, J.Y., Jang, I.K., Hodes, R., and Gu, H. (2007). Ablation of Cbl-b provides protection against transplanted and spontaneous tumors. J. Clin. Invest. *117*, 1029–1036.

Colaprico, A., Silva, T.C., Olsen, C., Garofano, L., Cava, C., Garolini, D., Sabedot, T.S., Malta, T.M., Pagnotta, S.M., Castiglioni, I., et al. (2016). TCGAbiolinks: an R/Bioconductor package for integrative analysis of TCGA data. Nucleic Acids Res. *44*, e71.

Croxford, J.L., Tang, M.L., Pan, M.F., Huang, C.W., Kamran, N., Phua, C.M., Chng, W.J., Ng, S.B., Raulet, D.H., and Gasser, S. (2013). ATM-dependent spontaneous regression of early Eμ-myc-induced murine B-cell leukemia depends on natural killer and T cells. Blood *121*, 2512–2521.

Díaz, L.R., Saavedra-López, E., Romarate, L., Mitxitorena, I., Casanova, P.V., Cribaro, G.P., Gallego, J.M., Pérez-Vallés, A., Forteza-Vila, J., Alfaro-Cervello, C., et al. (2018). Imbalance of immunological synapse-kinapse states reflects tumor escape to immunity in glioblastoma. JCI Insight *3*, e120757.

Dolgalev, I. (2019). msigdbr: MSigDB Gene Sets for Multiple Organisms in a Tidy Data Format. R package version 7.0.1. (R Project for Statistical Computing).

Durinck, S., Moreau, Y., Kasprzyk, A., Davis, S., De Moor, B., Brazma, A., and Huber, W. (2005). BioMart and Bioconductor: a powerful link between biological databases and microarray data analysis. Bioinformatics *21*, 3439–3440.

Durinck, S., Spellman, P.T., Birney, E., and Huber, W. (2009). Mapping identifiers for the integration of genomic datasets with the R/Bioconductor package biomaRt. Nat. Protoc. *4*, 1184–1191.

Dustin, M.L. (2014). The immunological synapse. Cancer Immunol. Res. *2*, 1023–1033.

Effern, M., Glodde, N., Braun, M., Liebing, J., Boll, H.N., Yong, M., Bawden, E., Hinze, D., van den Boorn-Konijnenberg, D., Daoud, M., et al. (2020). Adoptive T Cell Therapy Targeting Different Gene Products Reveals Diverse and Context-Dependent Immune Evasion in Melanoma. Immunity *53*, 564–580.e9.

Fay, C., Sidi, J., and Smith, L. (2018). remedy: 'RStudio' Addins to Simplify 'Markdown' Writing. R package version 0.1.0. (R Project for Statistical Computing).

Ferrari de Andrade, L., Ngiow, S.F., Stannard, K., Rusakiewicz, S., Kalimutho, M., Khanna, K.K., Tey, S.K., Takeda, K., Zitvogel, L., Martinet, L., and Smyth, M.J. (2014). Natural killer cells are essential for the ability of BRAF inhibitors to control BRAFV600E-mutant metastatic melanoma. Cancer Res. *74*, 7298–7308.

Gaud, G., Roncagalli, R., Chaoui, K., Bernard, I., Familiades, J., Colacios, C., Kassem, S., Monsarrat, B., Burlet-Schiltz, O., de Peredo, A.G., et al. (2018). The costimulatory molecule CD226 signals through VAV1 to amplify TCR signals and promote IL-17 production by $CD4^+$ T cells. Sci. Signal. *11*, eaar3083.

Gilfillan, S., Chan, C.J., Cella, M., Haynes, N.M., Rapaport, A.S., Boles, K.S., Andrews, D.M., Smyth, M.J., and Colonna, M. (2008). DNAM-1 promotes activation of cytotoxic lymphocytes by nonprofessional antigen-presenting cells and tumors. J. Exp. Med. *205*, 2965–2973.

Glodde, N., Bald, T., van den Boorn-Konijnenberg, D., Nakamura, K., O'Donnell, J.S., Szczepanski, S., Brandes, M., Eickhoff, S., Das, I., Shridhar, N., et al. (2017). Reactive Neutrophil Responses Dependent on the Receptor Tyrosine Kinase c-MET Limit Cancer Immunotherapy. Immunity *47*, 789–802.e9.

Gupta, P.K., Godec, J., Wolski, D., Adland, E., Yates, K., Pauken, K.E., Cosgrove, C., Ledderose, C., Junger, W.G., Robson, S.C., et al. (2015). CD39 Expression Identifies Terminally Exhausted CD8+ T Cells. PLoS Pathog. *11*, e1005177.

He, B., Xing, S., Chen, C., Gao, P., Teng, L., Shan, Q., Gullicksrud, J.A., Martin, M.D., Yu, S., Harty, J.T., et al. (2016). $CD8^+$ T Cells Utilize Highly Dynamic Enhancer Repertoires and Regulatory Circuitry in Response to Infections. Immunity *45*, 1341–1354.

Helmink, B.A., Gaudreau, P.O., and Wargo, J.A. (2018). Immune Checkpoint Blockade across the Cancer Care Continuum. Immunity *48*, 1077–1080.

Herneau, T. (2020). A Package for Survival Analysis in R. R package version 3.1-12. (R Project for Statistical Computing).

Hou, S., Ge, K., Zheng, X., Wei, H., Sun, R., and Tian, Z. (2014). CD226 protein is involved in immune synapse formation and triggers Natural Killer (NK) cell activation via its first extracellular domain. J. Biol. Chem. *289*, 6969–6977.

Huber, W., Carey, V.J., Gentleman, R., Anders, S., Carlson, M., Carvalho, B.S., Bravo, H.C., Davis, S., Gatto, L., Girke, T., et al. (2015). Orchestrating high-throughput genomic analysis with Bioconductor. Nat. Methods *12*, 115–121.

Iguchi-Manaka, A., Kai, H., Yamashita, Y., Shibata, K., Tahara-Hanaoka, S., Honda, S., Yasui, T., Kikutani, H., Shibuya, K., and Shibuya, A. (2008). Accelerated tumor growth in mice deficient in DNAM-1 receptor. J. Exp. Med. *205*, 2959–2964.

Jacobsen, A., and Luna, A. (2019). cgdsr: R-Based API for Accessing the MSKCC Cancer Genomics Data Server (CGDS) R package. (R Project for Statistical Computing).

Jin, H.S., Ko, M., Choi, D.S., Kim, J.H., Lee, D.H., Kang, S.H., Kim, I., Lee, H.J., Choi, E.K., Kim, K.P., et al. (2020). CD226(hi)CD8(+) T Cells Are a Prerequisite for Anti-TIGIT Immunotherapy. Cancer Immunol Res *204*, 165.10.

Johnston, R.J., Yu, X., and Grogan, J.L. (2015). The checkpoint inhibitor TIGIT limits antitumor and antiviral $CD8^+$ T cell responses. OncoImmunology *4*, e1036214.

Kamran, N., Takai, Y., Miyoshi, J., Biswas, S.K., Wong, J.S., and Gasser, S. (2013). Toll-like receptor ligands induce expression of the costimulatory molecule CD155 on antigen-presenting cells. PLoS ONE *8*, e54406.

Kassambara, A., Kosinski, M., and Bicek, P. (2019). survminer: Drawing Survival Curves using 'ggplot2'. R package version 0.4.6. (R Project for Statistical Computing).

Khan, O., Giles, J.R., McDonald, S., Manne, S., Ngiow, S.F., Patel, K.P., Werner, M.T., Huang, A.C., Alexander, K.A., Wu, J.E., et al. (2019). TOX transcriptionally and epigenetically programs $CD8^+$ T cell exhaustion. Nature *571*, 211–218.

Kim, J.S., Shin, B.R., Lee, H.K., Lee, J.H., Kim, K.H., Choi, J.E., Ji, A.Y., Hong, J.T., Kim, Y., and Han, S.B. (2017). *Cd226*$^{-/-}$ natural killer cells fail to establish stable contacts with cancer cells and show impaired control of tumor metastasis *in vivo*. OncoImmunology *6*, e1338994.

Lakshmikanth, T., Burke, S., Ali, T.H., Kimpfler, S., Ursini, F., Ruggeri, L., Capanni, M., Umansky, V., Paschen, A., Sucker, A., et al. (2009). NCRs and DNAM-1 mediate NK cell recognition and lysis of human and mouse melanoma cell lines in vitro and in vivo. J. Clin. Invest. *119*, 1251–1263.

Landsberg, J., Kohlmeyer, J., Renn, M., Bald, T., Rogava, M., Cron, M., Fatho, M., Lennerz, V., Wölfel, T., Hölzel, M., and Tüting, T. (2012). Melanomas resist T-cell therapy through inflammation-induced reversible dedifferentiation. Nature *490*, 412–416.

Lepletier, A., Lutzky, V.P., Mittal, D., Stannard, K., Watkins, T.S., Ratnatunga, C.N., Smith, C., McGuire, H.M., Kemp, R.A., Mukhopadhyay, P., et al. (2019). The immune checkpoint CD96 defines a distinct lymphocyte phenotype and is highly expressed on tumor-infiltrating T cells. Immunol. Cell Biol. *97*, 152–164.

Lepletier, A., Madore, J., O'Donnell, J.S., Johnston, R.L., Li, X.Y., McDonald, E., Ahern, E., Kuchel, A., Eastgate, M., Pearson, S.A., et al. (2020). Tumor CD155 expression is associated with resistance to anti-PD1 immunotherapy in metastatic melanoma. Clin. Cancer Res. *26*, 3671–3681.

Li, X.Y., Das, I., Lepletier, A., Addala, V., Bald, T., Stannard, K., Barkauskas, D., Liu, J., Aguilera, A.R., Takeda, K., et al. (2018). CD155 loss enhances tumor suppression via combined host and tumor-intrinsic mechanisms. J. Clin. Invest. *128*, 2613–2625.

Loeser, S., Loser, K., Bijker, M.S., Rangachari, M., van der Burg, S.H., Wada, T., Beissert, S., Melief, C.J., and Penninger, J.M. (2007). Spontaneous tumor rejection by cbl-b-deficient CD8+ T cells. J. Exp. Med. *204*, 879–891.

Manrique, S., Sauter, D., Horenkamp, F.A., Lülf, S., Yu, H., Hotter, D., Anand, K., Kirchhoff, F., and Geyer, M. (2017). Endocytic sorting motif interactions involved in Nef-mediated downmodulation of CD4 and CD3. Nat. Commun. *8*, 442.

Markey, K.A., Gartlan, K.H., Kuns, R.D., MacDonald, K.P., and Hill, G.R. (2015). Imaging the immunological synapse between dendritic cells and T cells. J. Immunol. Methods *423*, 40–44.

Martin, M. (2011). "Cutadapt removes adapter sequences from high-throughput sequencing reads.". EMBnet.journal *17* (1), 10–12.

Martinet, L., and Smyth, M.J. (2015). Balancing natural killer cell activation through paired receptors. Nat. Rev. Immunol. *15*, 243–254.

Mognol, G.P., Spreafico, R., Wong, V., Scott-Browne, J.P., Togher, S., Hoffmann, A., Hogan, P.G., Rao, A., and Trifari, S. (2017). Exhaustion-associated regulatory regions in CD8$^+$ tumor-infiltrating T cells. Proc. Natl. Acad. Sci. USA *114*, E2776–E2785.

Möller, A., House, C.M., Wong, C.S., Scanlon, D.B., Liu, M.C., Ronai, Z., and Bowtell, D.D. (2009). Inhibition of Siah ubiquitin ligase function. Oncogene *28*, 289–296.

Morgan, M., and Davis, S. (2019). GenomicDataCommons: NIH / NCI Genomic Data Commons Access R package. (Bioconductor).

Morgan, M., Obenchain, V., Hester, J., and Pagès, H. (2018). SummarizedExperiment: SummarizedExperiment container R package. (Bioconductor).

Mueller, K., and Walthert, L. (2020). styler: Non-Invasive Pretty Printing of R Code. R package version 1.3.2. (R Project for Statistical Computing).

Nabekura, T., Kanaya, M., Shibuya, A., Fu, G., Gascoigne, N.R., and Lanier, L.L. (2014). Costimulatory molecule DNAM-1 is essential for optimal differentiation of memory natural killer cells during mouse cytomegalovirus infection. Immunity *40*, 225–234.

Nakamura, K., Kassem, S., Cleynen, A., Chretien, M.L., Guillerey, C., Putz, E.M., Bald, T., Forster, I., Vuckovic, S., Hill, G.R., et al. (2018). Dysregulated IL-18 Is a Key Driver of Immunosuppression and a Possible Therapeutic Target in the Multiple Myeloma Microenvironment. Cancer Cell *33*, 634–648.e5.

O'Donnell, J.S., Teng, M.W.L., and Smyth, M.J. (2019). Cancer immunoediting and resistance to T cell-based immunotherapy. Nat. Rev. Clin. Oncol. *16*, 151–167.

O'Leary, C.E., Lewis, E.L., and Oliver, P.M. (2015). Ubiquitylation as a Rheostat for TCR Signaling: From Targeted Approaches Toward Global Profiling. Front. Immunol. *6*, 618.

Oksvold, M.P., Dagger, S.A., Thien, C.B., and Langdon, W.Y. (2008). The Cbl-b RING finger domain has a limited role in regulating inflammatory cytokine production by IgE-activated mast cells. Mol. Immunol. *45*, 925–936.

Pauken, K.E., and Wherry, E.J. (2014). TIGIT and CD226: tipping the balance between costimulatory and coinhibitory molecules to augment the cancer immunotherapy toolkit. Cancer Cell *26*, 785–787.

Putz, E.M., Guillerey, C., Kos, K., Stannard, K., Miles, K., Delconte, R.B., Takeda, K., Nicholson, S.E., Huntington, N.D., and Smyth, M.J. (2017). Targeting cytokine signaling checkpoint CIS activates NK cells to protect from tumor initiation and metastasis. OncoImmunology *6*, e1267892.

Raab, M., Wang, H., Lu, Y., Smith, X., Wu, Z., Strebhardt, K., Ladbury, J.E., and Rudd, C.E. (2010). T cell receptor "inside-out" pathway via signaling module SKAP1-RapL regulates T cell motility and interactions in lymph nodes. Immunity *32*, 541–556.

Ralston, K.J., Hird, S.L., Zhang, X., Scott, J.L., Jin, B., Thorne, R.F., Berndt, M.C., Boyd, A.W., and Burns, G.F. (2004). The LFA-1-associated molecule PTA-1 (CD226) on T cells forms a dynamic molecular complex with protein 4.1G and human discs large. J. Biol. Chem. *279*, 33816–33828.

Ramsbottom, K.M., Hawkins, E.D., Shimoni, R., McGrath, M., Chan, C.J., Russell, S.M., Smyth, M.J., and Oliaro, J. (2014). Cutting edge: DNAX accessory molecule 1-deficient CD8+ T cells display immunological synapse defects that impair antitumor immunity. J. Immunol. *192*, 553–557.

Riesenberg, S., Groetchen, A., Siddaway, R., Bald, T., Reinhardt, J., Smorra, D., Kohlmeyer, J., Renn, M., Phung, B., Aymans, P., et al. (2015). MITF and c-Jun antagonism interconnects melanoma dedifferentiation with pro-inflammatory cytokine responsiveness and myeloid cell recruitment. Nat. Commun. *6*, 8755.

Schmid-Burgk, J.L., Schmidt, T., Gaidt, M.M., Pelka, K., Latz, E., Ebert, T.S., and Hornung, V. (2014). OutKnocker: a web tool for rapid and simple genotyping of designer nuclease edited cell lines. Genome Res. *24*, 1719–1723.

Schmid-Burgk, J.L., Höning, K., Ebert, T.S., and Hornung, V. (2016). CRISPaint allows modular base-specific gene tagging using a ligase-4-dependent mechanism. Nat. Commun. *7*, 12338.

Schreiber, R.D., Old, L.J., and Smyth, M.J. (2011). Cancer immunoediting: integrating immunity's roles in cancer suppression and promotion. Science *331*, 1565–1570.

Scott, A.C., Dündar, F., Zumbo, P., Chandran, S.S., Klebanoff, C.A., Shakiba, M., Trivedi, P., Menocal, L., Appleby, H., Camara, S., et al. (2019). TOX is a critical regulator of tumour-specific T cell differentiation. Nature *571*, 270–274.

Sergushichev, A.A. (2016). An algorithm for fast preranked gene set enrichment analysis using cumulative statistic calculation. bioRxiv. https://doi.org/10.1101/060012.

Seth, S., Qiu, Q., Danisch, S., Maier, M.K., Braun, A., Ravens, I., Czeloth, N., Hyde, R., Dittrich-Breiholz, O., Förster, R., and Bernhardt, G. (2011). Intranodal interaction with dendritic cells dynamically regulates surface expression of the co-stimulatory receptor CD226 protein on murine T cells. J. Biol. Chem. *286*, 39153–39163.

Shibuya, A., Campbell, D., Hannum, C., Yssel, H., Franz-Bacon, K., McClanahan, T., Kitamura, T., Nicholl, J., Sutherland, G.R., Lanier, L.L., and Phillips, J.H. (1996). DNAM-1, a novel adhesion molecule involved in the cytolytic function of T lymphocytes. Immunity *4*, 573–581.

Shibuya, A., Lanier, L.L., and Phillips, J.H. (1998). Protein kinase C is involved in the regulation of both signaling and adhesion mediated by DNAX accessory molecule-1 receptor. J. Immunol. *161*, 1671–1676.

Shibuya, K., Lanier, L.L., Phillips, J.H., Ochs, H.D., Shimizu, K., Nakayama, E., Nakauchi, H., and Shibuya, A. (1999). Physical and functional association of LFA-1 with DNAM-1 adhesion molecule. Immunity *11*, 615–623.

Shibuya, K., Shirakawa, J., Kameyama, T., Honda, S., Tahara-Hanaoka, S., Miyamoto, A., Onodera, M., Sumida, T., Nakauchi, H., Miyoshi, H., and Shibuya, A. (2003). CD226 (DNAM-1) is involved in lymphocyte function-associated antigen 1 costimulatory signal for naive T cell differentiation and proliferation. J. Exp. Med. *198*, 1829–1839.

Shirakawa, J., Shibuya, K., and Shibuya, A. (2005). Requirement of the serine at residue 329 for lipid raft recruitment of DNAM-1 (CD226). Int. Immunol. *17*, 217–223.

Shirakawa, J., Wang, Y., Tahara-Hanaoka, S., Honda, S., Shibuya, K., and Shibuya, A. (2006). LFA-1-dependent lipid raft recruitment of DNAM-1 (CD226) in CD4+ T cell. Int. Immunol. *18*, 951–957.

Shiratori, T., Miyatake, S., Ohno, H., Nakaseko, C., Isono, K., Bonifacino, J.S., and Saito, T. (1997). Tyrosine phosphorylation controls internalization of CTLA-4 by regulating its interaction with clathrin-associated adaptor complex AP-2. Immunity *6*, 583–589.

Singer, M., Wang, C., Cong, L., Marjanovic, N.D., Kowalczyk, M.S., Zhang, H., Nyman, J., Sakuishi, K., Kurtulus, S., Gennert, D., et al. (2016). A Distinct Gene Module for Dysfunction Uncoupled from Activation in Tumor-Infiltrating T Cells. Cell *166*, 1500–1511.e9.

Stoeckius, M., Hafemeister, C., Stephenson, W., Houck-Loomis, B., Chattopadhyay, P.K., Swerdlow, H., Satija, R., and Smibert, P. (2017). Simultaneous epitope and transcriptome measurement in single cells. Nat. Methods *14*, 865–868.

Stuart, T., Butler, A., Hoffman, P., Hafemeister, C., Papalexi, E., Mauck, W.M., 3rd, Hao, Y., Stoeckius, M., Smibert, P., and Satija, R. (2019). Comprehensive Integration of Single-Cell Data. Cell *177*, 1888–1902.e21.

Tahara-Hanaoka, S., Shibuya, K., Onoda, Y., Zhang, H., Yamazaki, S., Miyamoto, A., Honda, S., Lanier, L.L., and Shibuya, A. (2004). Functional characterization of DNAM-1 (CD226) interaction with its ligands PVR (CD155) and nectin-2 (PRR-2/CD112). Int. Immunol. *16*, 533–538.

Tahara-Hanaoka, S., Shibuya, K., Kai, H., Miyamoto, A., Morikawa, Y., Ohkochi, N., Honda, S., and Shibuya, A. (2006). Tumor rejection by the poliovirus receptor family ligands of the DNAM-1 (CD226) receptor. Blood *107*, 1491–1496.

Thelen, M., Lechner, A., Wennhold, K., von Bergwelt-Baildon, M., and Schlößer, H.A. (2018). CD39 Expression Defines Cell Exhaustion in Tumor-Infiltrating CD8$^+$ T Cells-Letter. Cancer Res. *78*, 5173–5174.

Thommen, D.S., and Schumacher, T.N. (2018). T Cell Dysfunction in Cancer. Cancer Cell *33*, 547–562.

Ushey, K., Allaire, J., Wickham, H., and Ritchie, G. (2020). rstudioapi: Safely Access the RStudio API. R package version 0.11. (MIT).

Vo, A.V., Takenaka, E., Shibuya, A., and Shibuya, K. (2016). Expression of DNAM-1 (CD226) on inflammatory monocytes. Mol. Immunol. *69*, 70–76.

Wang, B., Zhang, W., Jankovic, V., Golubov, J., Poon, P., Oswald, E.M., Gurer, C., Wei, J., Ramos, I., Wu, Q., et al. (2018). Combination cancer immunotherapy targeting PD-1 and GITR can rescue CD8$^+$ T cell dysfunction and maintain memory phenotype. Sci. Immunol. *3*, eaat7061.

Wang, X., He, Q., Shen, H., Xia, A., Tian, W., Yu, W., and Sun, B. (2019). TOX promotes the exhaustion of antitumor CD8$^+$ T cells by preventing PD1 degradation in hepatocellular carcinoma. J. Hepatol. *71*, 731–741.

Warnes, G.R., Bolker, B., Bonebakker, L., Gentleman, R., Huber, W., Liaw, A., Lumley, T., Maechler, M., Magnusson, A., Moeller, S., Schwartz, M., and Venables, B. (2019). gplots: Various R Programming Tools for Plotting Data R package. (R Project for Statistical Computing).

Weulersse, M., Asrir, A., Pichler, A.C., Lemaitre, L., Braun, M., Carrié, N., Joubert, M.-V., Le Moine M, Do Souto, L., Gaud, G., et al. (2020). Eomes-dependent loss of the co-activating receptor CD226 restrains CD8$^+$ T cell anti-tumor functions and limits the efficacy of cancer immunotherapy. Immunity *53*. Published online October 13, 2020. https://doi.org/10.1016/j.immuni.2020.09.006.

Wherry, E.J., and Kurachi, M. (2015). Molecular and cellular insights into T cell exhaustion. Nat. Rev. Immunol. *15*, 486–499.

Wickham, H. (2016). ggplot2: Elegant Graphics for Data Analysis R package. (Springer-Verlag).

Wickham, H. (2019). stringr: Simple, Consistent Wrappers for Common String Operations. R package version 1.4.0. (Rstudio).

Wickham, H., Francois, R., Henry, L., and Mueller, K. (2020). dplyr: A Grammar of Data Manipulation. R package. (R Project for Statistical Computing).

Wilke, C. (2019). cowplot: Streamlined Plot Theme and Plot Annotations for 'ggplot2'. R package version 1.0.0. (R Project for Statistical Computing).

Yu, G., Wang, L.G., Han, Y., and He, Q.Y. (2012). clusterProfiler: an R package for comparing biological themes among gene clusters. OMICS *16*, 284–287.

Zhang, Z., Wu, N., Lu, Y., Davidson, D., Colonna, M., and Veillette, A. (2015). DNAM-1 controls NK cell activation via an ITT-like motif. J. Exp. Med. *212*, 2165–2182.

Xie, Y. (2020). knitr: A General-Purpose Package for Dynamic Report Generation in R. R package version 1.28. (R Project for Statistical Computing).

## STAR★METHODS

### KEY RESOURCES TABLE

| REAGENT or RESOURCE | SOURCE | IDENTIFIER |
|---|---|---|
| Antibodies | | |
| FITC anti-mouse CD3 (clone 17A2) | ebioscience | Cat#: 11-0032-82 RRID: AB_2572431 |
| APC-eF780 anti-mouse CD3 (clone 17A2) | ebioscience | Cat#: 47-0032-82 RRID: AB_1272181 |
| BV421 anti-mouse CD28 (clone 37.51) | Biolegend | Cat#: 102127 RRID:AB_2650628 |
| APC anti-mouse CD28 (clone 37.51) | ebiscience | Cat#: 17-0281-82 RRID:AB_469374 |
| AF647 anti-mouse CD226 (DNAM-1) (clone 10E5) | Biolegend | Cat#: 128808 RRID:AB_1227541 |
| PE anti-mouse CD226 (DNAM-1) (clone 480.1) | Biolegend | Cat#: 132006 RRID:AB_1279173 |
| PE-Cy7 anti-mouse CD226 (DNAM-1) (clone 10E5) | Biolegend | Cat#: 128812 RRID:AB_2566629 |
| APC anti-mouse CD226 (DNAM-1) (clone 10E5) | Biolegend | Cat#: 128810 RRID:AB_2566627 |
| APC anti-mouse CD8a (clone 53-6.7) | Biolegend | Cat#: 100712 RRID:AB_312751 |
| BV421 anti-mouse CD8a (clone 53-6.7) | Biolegend | Cat#: 100738 RRID:AB_11204079 |
| BV711 anti-mouse CD8a (clone 53-6.7) | Biolegend | Cat#: 100748 RRID:AB_2562100 |
| BV785 anti-mouse CD8a (clone 53-6.7) | Biolegend | Cat#: 100749 RRID:AB_11218801 |
| APC anti-mouse IFN-γ (clone XMG1.2) | Biolegend | Cat#: 505810 RRID: AB_315404 |
| PE anti-mouse IFN-γ (clone XMG1.2) | ebioscience | Cat#: 12-7311-82 RRID: AB_466193 |
| BV605 anti-mouse TNF-α (clone MP6-XT22) | Biolegend | Cat#:506329 RRID: AB_11123912 |
| Pacific Blue anti-mouse Granzyme-B (clone GB11) | Biolegend | Cat#:515408 RRID: AB_2562196 |
| BUV-395 anti-mouse Ki67 (clone B56) | BD biosciences | Cat#:564071 RRID: AB_2738577 |
| APC anti-mouse Ki67 (clone 16A8) | Biolegend | Cat#:652406 RRID: AB_2561930 |
| eFlour 450 anti-mouse Ki67 (clone SolA15) | ebioscience | Cat#:48-5698-82 RRID: AB_11149124 |
| PE anti-mouse Bcl-2 (clone BCL/10C4) | Biolegend | Cat#:633507 RRID: AB_2043939 |
| PE-Cy7 anti-mouse CD279 (PD-1) (clone J43) | ebioscience | Cat#:25-9985-82 RRID: AB_10853805 |
| BV 605 anti-mouse CD279 (PD-1) (clone 29F.IA12) | Biolegend | Cat#:135220 RRID: AB_2562616 |
| BV 785 anti-mouse CD279 (PD-1) (clone 29F.IA12) | Biolegend | Cat#:135225 RRID: AB_2563680 |
| APC anti-mouse CD96 (TACTILE) (clone 3.3) | Biolegend | Cat#:131712 RRID: AB_2650741 |
| PE anti-mouse CD96 (TACTILE) (clone 3.3) | Biolegend | Cat#:131706 RRID: AB_2076169 |
| BV421 anti-mouse CD96 (TACTILE) (clone 6A6) | BD biosciences | Cat#:565687 RRID: AB_2739329 |
| PerCP/Cy5.5 anti-mouse CD223 (LAG-3) (clone C9B7W) | Biolegend | Cat#:125212 RRID: AB_2561517 |

(*Continued on next page*)

*Continued*

| REAGENT or RESOURCE | SOURCE | IDENTIFIER |
|---|---|---|
| APC anti-mouse CD223 (LAG-3) (clone C9B7W) | Biolegend | Cat#:125210 RRID: AB_10639727 |
| BV421 anti-mouse TIGIT (Vstm-3) (clone 1G9) | Biolegend | Cat#:142111 RRID: AB_2687311 |
| APC anti-mouse TIGIT (Vstm-3) (clone 1G9) | Biolegend | Cat#:142106 RRID: AB_10962572 |
| BV605 anti-mouse CD366 (Tim-3) (clone RMT3-23) | Biolegend | Cat#:119721 RRID: AB_2616907 |
| PE/Cy7 anti-mouse CD39 (clone 24DMS1) | eBioscience | Cat#:25-0391-82 RRID: AB_1210766 |
| APC-eF780 anti-mouse CD45-2 (clone 104) | ebioscience | Cat#:47-0454-82 RRID: AB_1272175 |
| APC anti-mouse CD155 (PVR) (clone TX56) | Biolegend | Cat#:131510 RRID:AB_10645507 |
| V450 anti-mouse Vb13 TCR (clone MR12) | BD biosciences | Cat#:3561539 RRID |
| APC anti-mouse TCR vbeta 13 (clone MR12) | eBioscience | Cat#:317-5797-80 RRID |
| Pacific Blue anti-mouse CD90.1 (clone OX-7) | Biolegend | Cat#:202522 RRID:AB_195477 |
| Alexa Fluor 700 anti-mouse CD90.1 (clone OX-7) | Biolegend | Cat#:202528 RRID:AB_1626241 |
| BV421 anti-mouse CD44 (clone IM7) | Biolegend | Cat#:103040 RRID:AB_2616903 |
| APC anti-mouse CD44 (clone IM7) | Biolegend | Cat#:103012 RRID:AB_312963 |
| FITC anti-mouse CD62L (clone MEL-14) | Biolegend | Cat#:104406 RRID:AB_313093 |
| PE/Cy7 anti-mouse CD62L (clone MEL-14) | Biolegend | Cat#:104418 RRID:AB_313103 |
| BV421 anti-mouse CD3e (clone 145-2C11) | Biolegend | Cat#:100336 RRID:AB_11203705 |
| APC-eFluor 780 anti-mouse CD3e (clone 145-2C11) | eBioscience | Cat#:47-0031-82 RRID:AB_11149861 |
| PerCP/Cy5.5 anti-mouse CD11a/CD18 (LFA-1) (clone H155-78) | Biolegend | Cat#: 141007 RRID:AB_10694861 |
| PE/Cy7 anti-mouse CD11a/CD18 (LFA-1) (clone H155-78) | Biolegend | Cat#: 141011 RRID: AB_2564307 |
| APC Streptavidin | BioLegend | Cat#: 405207 |
| Purified anti-mouse CD3 (clone 1455-2C11) | Biolegend | Cat#: 100302 RRID: AB_312667 |
| Purified anti-mouse CD28 (clone 37.51) | Biolegend | Cat#: 102102 RRID:AB_312867 |
| TotalSeq™-A0852 anti-mouse CD226 (clone 10E5) | Biolegend | Cat#: 128823 RRID:AB_2810393 |
| BV510 anti-human CD45 (clone HI30) | Biolegend | Cat#: 304035 RRID: AB_2561383 |
| AF700 anti-human CD45 (clone 2D1) | Biolegend | Cat#: 368513 RRID: AB_2566373 |
| V500 anti-human CD45 (clone: HI30) | BD Biosciences | Cat#: 560777 RRID: AB_1937324 |
| BV650 anti-human TNF-α (clone Mab11) | Biolegend | Cat#: 502937 RRID: AB_2561355 |
| BV785 anti-human CD226 (clone 11A8) | Biolegend | Cat#: 338321 RRID: AB_2721559 |

(*Continued on next page*)

*Continued*

| REAGENT or RESOURCE | SOURCE | IDENTIFIER |
|---|---|---|
| PE/Cy7 anti-human CD226 (DNAM-1) (clone 11A8) | Biolegend | Cat#: 338316 RRID: AB_2616645 |
| BUV737 anti-human CD3 (clone SK7) | BD Biosciences | Cat#: 565466 |
| PerCP/Cy5.5 anti-human CD3 (clone HIT3) | Biolegend | Cat#: 300328 RRID: AB_1575010 |
| FITC anti-human CD8 (clone RPA-T8) | Biolegend | Cat#: 301006 RRID: AB_314124 |
| AF700 anti-human CD8 (clone SK1) | Biolegend | Cat#: 344723 RRID: AB_2562789 |
| APC anti-human CD155 (clone SKII.4) | Biolegend | Cat#: 338316 RRID: AB_2616645 |
| FITC anti-human CD279 (PD-1) (clone MIH4) | BD Biosciences | Cat#: 557890 |
| BV711 anti-human CD39 (clone A1) | Biolegend | Cat#: 328228 RRID: AB_2632893 |
| PE-Dazzle 594 anti-human IFN-γ (clone B27) | Biolegend | Cat#: 506530 RRID: AB_2566717 |
| AF488 anti-human Ki67 | Biolegend | Cat#: 350508 RRID: AB_10933085 |
| PE anti-human CD107a (clone H4A3) | Biolegend | Cat#: 328608 RRID: AB_1186040 |
| Purified anti-human CD3 (clone OKT3) | Biolegend | Cat#: 317315; RRID: AB_1877070 |
| Purified anti-human CD226 (clone DX11) | BD | Cat#: 559786; RRID: AB_397327 |
| Rabbit monoclonal to human CD226 (clone 102) | Sino Biological | Cat#: 10565-R102; RRID: AB_2860200 |
| Mouse monoclonal to human CD8 (clone C8/144B) | DAKO | Cat#: M7103; RRID: AB_2075537 |
| Mouse monoclonal to human SOX10 (clone BC34) | Biocare Medical | Cat#: ACI3099A |
| Rabbit monoclonal to human CD155 (clone D3G7H) | CST | Cat#: 13544; RRID: AB_2798252 |
| Rabbit anti-mouse CD226 (clone EPR20710) | Abcam | Cat#: ab212077 |
| Mouse anti-ubiquitin (clone Ubi-1) | Invitrogen | Cat#: 13-1600; RRID: AB_2533002 |
| Mouse anti-Cbl-b (clone G-1) | Santa Cruz Biotechnology | Cat#: sc-8006; RRID: AB_626816 |
| Rabbit anti-β-actin (polyclonal) | Cell Signaling Technology | Cat#: 4967; RRID: AB_330288 |
| Mouse anti-α-tubulin (clone DM1A) | Sigma | Cat#: T9026; RRID: AB_477593 |
| HRP Goat anti-rabbit IgG (H+L) (polyclonal) | Invitrogen | Cat#: 31460 |
| HRP Goat anti-mouse IgG (H+L) (polyclonal) | Invitrogen | Cat#: 31430 |
| Mouse anti-human Isotype IgG1, clone MOPC-21 | Biolegend | Cat#: 400153 |
| Rat-control Isotype IgG2a, clone 1-1 | Leinco | Cat#: R1367; RRID: AB_2831721 |
| Rat-anti-mouse PD-1 IgG2a, clone RMP 1-14 | BioXCell | Cat#: BE0146; RRID: AB_10949053 |
| Polyclonal Hamster-control IgG | BioXCell | Cat#: BE0091; RRID: AB_1107773 |
| Hamster-anti-mouse CTLA4, clone UC10-4F10-11 | BioXCell | Cat#: BE0032; RRID: AB_1107598 |
| Rat-anti-mouse CD155 IgG2a, clone 4.24 | Leinco | Cat#: C2833; RRID: AB_2737472 |
| Rat-anti mouse CD226, IgG2a, clone 480 | produced in-house | N/A |
| Bacterial and Virus Strains | | |
| Competent E.coli bacteria strain XL10Blue | produced in-house | N/A |
| Competent E.coli bacteria strain BL21 (DE3) | NEB | N/A |

(*Continued on next page*)

*Continued*

| REAGENT or RESOURCE | SOURCE | IDENTIFIER |
|---|---|---|
| Biological Samples | | |
| Human metastatic melanoma tissue microarray (Sydney Cohort) | Melanoma Institute Australia | MIA-18_001_3A |
| Human metastatic melanoma tissue microarray (Bonn Cohort) | University Hospital Bonn, Germany | N/A |
| Human metastatic melanoma specimens (St. Gallen Cohort) | Kanton Spital St. Gallen, Switzerland | N/A |
| HNSCC tumor specimens | Oral and Maxillofacial Department, Metro North HHS, Pathology Queensland-Anatomical Pathology, Royal Brisbane and Women's Hospital, Herston, Queensland, Australia | N/A |
| Healthy donor PBMCs | Australian *Red Cross* Blood Service Material Supply / Agreement No. 18-05QLD014 | N/A |
| Chemicals, Peptides, and Recombinant Proteins | | |
| PP2, src-kinase inhibitor | Sellekchem | Cat#: S7008 |
| PP2, src-kinase inhibitor | Millipore | Cat#: 529573-1MG |
| Dynasore, Dynamin Inhibitor | Sellekchem | Cat#: S8047 |
| PitStop2, Clathrin inhibitor | Abcam | Cat#: ab120687 |
| MG132, proteasome inhibitor | Sigma | Cat#: M7449 |
| Live/dead NIR | ThermoFisher Scientific | Cat#: L10119 |
| Zombie Aqua™ Fixable Viability Kit | Biolegend | Cat#: 423102 |
| Phalloidin AF647 | Invitrogen | Cat#: A22287 |
| Polybrene | Sigma | Cat#: TR-1003 |
| Triton-X | Sigma | Cat#: T8787 |
| Fugene 6 | Promega | Cat#: E2691 |
| human $gp100_{25-33}$ peptide (aa: KVPRNQDWL) | Mimotopes Pty LTD, Mulgrave, Victoria, Australia | Custom Peptide Synthesis |
| CHO complete medium | Thermo Fisher | Cat#: 10743011 |
| Hypoxanthine, Thymidine | Corning | Cat#: 25-047-CI |
| Collagenase D | Sigma | Cat#: 11088858001 |
| DNase I | Roche | Cat#: 4536282001 |
| RetroNectin (recombinant human fibronectin fragment) | Takara Bio Inc. | Cat#: T100A |
| recombinant mouse CD155-Fc | Sino Biological | Cat#: 50259-M03H |
| human IgG1 Isotype | BioXCell | Cat#: BE0297 |
| recombinant human IL-2 | Peprotech | Cat#: 200-02 |
| recombinant human IL-2 | Novartis | Cat#: C168171-01 |
| recombinant murine GM-CSF | Miltenyi Biotec | Cat#: 130-095-746 |
| recombinant murine IL-7 | R&D Systems | Cat#: 407-ML |
| recombinant murine IL-2 | Peprotech | Cat#: 212-12 |
| Cyclophosphamide | Baxter | Cat#: 2638B3847 |
| PolyI:C (HMW) | Invivogen | Cat#: tlrl-pic |
| 3-Methylcholanthrene | Sigma | Cat#: 213942 |
| Dako Target Retrieval Solution ph 9, 10x | DAKO Agilent | Cat#: S236784-2 |
| DAB Chromogen Kit | Biocare | Cat#: BDB2004 |
| Antibody diluent DaVinci Green | Biocare | Cat#: PD900L |
| Van Gogh Yellow Diluent | Biocare | Cat#: PD902 |
| Background Sniper | Biocare | Cat#: BS966L |
| MACH 3 Rabbit HRP Polymer detection kit | Biocare | Cat#: M3R531L |
| Opal Polymer HRP Ms plus Rb,1x | Perkin Elmer | Cat#: ARH1001EA |

(*Continued on next page*)

*Continued*

| REAGENT or RESOURCE | SOURCE | IDENTIFIER |
|---|---|---|
| OPAL 7-color automation IHC kit | Perkin Elmer | Cat#: NEL821001KT |
| RLT lysis buffer | QIAGEN | Cat#: 79216 |
| Kb-OVA biotinylated monomers | Purchased from Prof Andrew Brooks, Department of Microbiology and Immunology, Peter Doherty Institute, University of Melbourne, Melbourne, Australia | N/A |
| cOmplete™ Protease Inhibitor Cocktail | Roche | Cat#: 4693116001 |
| Bicinchoninic Acid (BCA) Kit for Protein Determination | Sigma | Cat#: BCA1 |
| 2-Mercaptoethanol | Sigma | Cat#: M3148 |
| Amersham™ ECL™ Select | GE Healthcare | Cat#: GERPN2235 |
| Ni Sepharose® 6Fast Flow | GE Healthcare | Cat#: 17-5318-01 |
| IRS-1 (Cblin) - DG**Y**MP | GenScript | N/A |
| ZAP70 (S) - DG**Y**TPEPA | GenScript | N/A |
| ZAP70 (L) - TLNSDG**Y**TPEPAR | GenScript | N/A |
| CD226$^{mpY319}$ - TLNSDG**Y**TPEPAR | GenScript | N/A |
| CD226 $^{mpY319F}$ - DTREDIFVNYPTF | GenScript | N/A |
| CD226 $^{hpY319}$ - DEKEDI**Y**VNYPTF | GenScript | N/A |
| CD226 $^{hY319}$ - DEKEDIYVNYPTF | GenScript | N/A |
| CD226 $^{hY319F}$ - DEKEDIFVNYPTF | N/A | N/A |
| Critical Commercial Assays | | |
| Plasmid Midi Purification Kit | Invitrogen | Cat#: K210004 |
| RNA Easy | QIAGEN | Cat#: 74104 |
| Lenti-X Single Shot packaging system | Clontech | Cat#: 631276 |
| CD8a$^+$ T Cell Isolation Kit, mouse | Miltenyi Biotec | Cat#: 130-104-075 |
| EasySep™ Mouse CD8+ T Cell Isolation Kit | StemCell | Cat#: 19853 |
| EasySep™ Mouse NK Cell Enrichment Kit | StemCell | Cat#: 19755 |
| RosetteSep human T cell enrichment cocktail | Stemcell | Cat#: 15061 |
| CD8$^+$ T Cell Isolation Kit, human | Miltenyi Biotec | Cat#: 130-096-495 |
| CD8 MicroBeads, human | Miltenyi Biotec | Cat#: 130-045-201 |
| Tumor Dissociation Kit | Miltenyi Biotec | Cat#:130-095-929 |
| Mouse/Rat Soluble Protein Master Buffer Kit | BD Biosciences | Cat#: 558266 |
| Mouse IFN-Gma CBA Flex Set A4 | BD Biosciences | Cat#: 558296 |
| BD Cytofix/Cytoperm | BD | Cat#: 554714 |
| FoxP3 Fix/Perm Buffer Set | Biolegend | Cat#: 421403 |
| BD GolgiPlug (containing Brefeldin A) | BD | Cat#: 555029 |
| Cell Stimulation Cocktail (plus protein transport inhibitors) | eBioscience | Cat#:00-4975-03 |
| Dynabeads Human T-Activator CD3/CD28 | ThermoFisher Scientific | Cat#: 111.31D |
| ImmunoCult Human CD3/CD28 T Cell Activator | Stemcell | Cat#: 10991 |
| Dynabeads Antibody Coupling Kit | Invitrogen | Cat#: 14311D |
| iScript cDNA Synthesis Kit | Bio Rad | Cat#: 1708891 |
| Protein A/G PLUS-Agarose Immunoprecipitation Reagent | Santa Cruz Biotechnology | Cat#: sc-2003 |
| NextSeq 500/550 High Output Kit v2.5 (150 cycles) | Illumina | Cat#: 20024907 |
| Chromium™ Chip B Single Cell Kit 16 rxn | Decode Science | Cat#: 10x-1000074 |
| Single Cell 3¢ Library GEL kit v3 | Decode Science | Cat#: 10x-1000092 |

(*Continued on next page*)

*Continued*

| REAGENT or RESOURCE | SOURCE | IDENTIFIER |
|---|---|---|
| Deposited Data | | |
| Single cell RNA sequencing dataset - accession number EGAS00001004423 | N/A | https://www.ebi.ac.uk/ega/ |
| Experimental Models: Cell Lines | | |
| Mouse B16F10 (melanoma) | QIMR Berghofer, Brisbane, Australia; M.J.S. laboratory (originally obtained from the ATCC) | N/A |
| B16F10$^{Ctrl}$ (melanoma) | QIMR Berghofer, Brisbane, Australia; M.J.S. laboratory | (Li et al., 2018) |
| B16F10$^{Cd155-/-}$ (melanoma) | QIMR Berghofer, Brisbane, Australia; M.J.S. laboratory | (Li et al., 2018) |
| Mouse MC38 (colon adenocarcinoma) | QIMR Berghofer, Brisbane, Australia; M.J.S. laboratory | (Gilfillan et al., 2008) |
| MC38-OVA$^{dim}$ (colon adenocarcinoma) | QIMR Berghofer, Brisbane, Australia; M.J.S. laboratory | (Gilfillan et al., 2008) |
| MC38-OVA$^{hi}$ (colon adenocarcinoma) | QIMR Berghofer, Brisbane, Australia; M.J.S. laboratory | (Gilfillan et al., 2008) |
| Mouse RM-1 (prostate carcinoma) | QIMR Berghofer, Brisbane, Australia; M.J.S. laboratory | (Blake et al., 2016) |
| Mouse LWT1 (melanoma) | QIMR Berghofer, Brisbane, Australia; M.J.S. laboratory | (Ferrari de Andrade et al., 2014) |
| Mouse HCmel12$^{hgp100}$ (melanoma) | Generated in the laboratory of M.H., Institute of Experimental Oncology, University of Bonn | (Effern et al., 2020) |
| Mouse Vk*MYC Vk12598 (multiple myeloma) | QIMR Berghofer, Brisbane, Australia; M.J.S. laboratory | (Nakamura et al., 2018) |
| Mouse Hepa 1-6 (hepatocellular carcinoma) | Kind gift from Prof. G. Anderson, QIMR Berghofer, Brisbane, Australia | N/A |
| Mouse RMA-S (lymphoma) | QIMR Berghofer, Brisbane, Australia; M.J.S. laboratory | (Zhang et al., 2015; Putz et al., 2017) |
| HEK293T cells | Kind gift from A/Prof Steven Lane, QIMR Berghofer, Brisbane, Australia | N/A |
| CHO-OKT3 subclone 2E5 | Immuno-Oncology Discovery, Bristol-Myers Squibb, Redwood City, California, USA | N/A |
| CHO-OKT3-CD155 | Immuno-Oncology Discovery, Bristol-Myers Squibb, Redwood City, California, USA | this paper |
| Jurkat E6.1 | Immuno-Oncology Discovery, Bristol-Myers Squibb, Redwood City, California, USA | N/A |
| Human YT-S-m*Cd226*$^{WT}$ (NK cell line) | IRCM, Montreal, QC, Canada; Veillette laboratory | (Zhang et al., 2015) |
| Mouse RMA-S-CD155$^{-}$ (lymphoma) | IRCM, Montreal, QC, Canada; Veillette laboratory | (Zhang et al., 2015) |
| Mouse RMA-S-CD155$^{+}$ (lymphoma) | IRCM, Montreal, QC, Canada; Veillette laboratory | (Zhang et al., 2015) |
| Experimental Models: Mice | | |
| Wild-type (WT) C57BL/6 | Walter and Eliza Hall Institute for Medical Research or bred in house, or IRCM animal facility | N/A |
| C57BL6 Pmel-1 TCRtg GFP mice | bred in house maintained at the QIMR Berghofer Medical Research Institute | (Glodde et al., 2017) |
| C57BL/6 CD226-deficient (*Cd226*$^{-/-}$) mice | bred in house maintained at the QIMR Berghofer Medical Research Institute | (Gilfillan et al., 2008) |

(*Continued on next page*)

*Continued*

| REAGENT or RESOURCE | SOURCE | IDENTIFIER |
|---|---|---|
| C57BL/6 *Cd226*$^{-/-}$.Pmel-1 TCRtg GFP mice | bred in house maintained at the QIMR Berghofer Medical Research Institute | this paper |
| C57BL/6 *Cd226*$^{-/-}$.Pmel-1 TCRtg mice | bred in house maintained at the QIMR Berghofer Medical Research Institute | this paper |
| C57BL/6 *Cd226*$^{Y319F}$ mice | bred in house maintained at the QIMR Berghofer Medical Research Institute, or IRCM animal facility | (Zhang et al., 2015) |
| C57BL/6 CD155-deficient (*Cd155*$^{-/-}$) | bred in house maintained at the QIMR Berghofer Medical Research Institute | (Li et al., 2018) |
| C57BL/6 *Cd226*$^{Y319F}$.Pmel-1 TCRtg GFP mice | bred in house maintained at the QIMR Berghofer Medical Research Institute | this paper |
| C57BL/6 *Cbl-b*$^{C373A}$ (*Cbl-b*$^{\Delta R}$) | obtained from the University of Western Australia | (Oksvold et al., 2008) |
| Oligonucleotides | | |
| CPG Oligo 1826; 5′-T*C*C*A*T*G*A*C*G*T*T*C*C*T*G*A*C*G*T*T-3′ | Biomers | custom oligonucleotide synthesis |
| Mouse *Cd226* Fwd "CATAACTTAACCCAGGTGGAGTG" | Integrated DNA Technologies, Baulkham Hills, Australia | this paper |
| Mouse *Cd226* Rev "ATGTCTGCTTCTGAGGCATTGTA" | Integrated DNA Technologies, Baulkham Hills, Australia | this paper |
| Recombinant DNA | | |
| MSCV-IRES-GFP | Kind gift from A/Prof Steven Lane, QIMR Berghofer, Brisbane, Australia | Addgene #20672 |
| Human PVR VersaClone cDNA | R&D Systems | Cat#: RDC1289 |
| pLenti-EF1a-C-mGFP Tagged Cloning Vector | Origene | Cat#: PS100084 |
| MSCV-IRES-GFP-mouse-*Cd226*$^{WT}$ | synthesized and cloned by BioMatik, Cambridge, Ontario, Canada | this paper |
| MSCV-IRES-GFP-human-*CD226*$^{WT}$ | synthesized and cloned by BioMatik, Cambridge, Ontario, Canada | this paper |
| MSCV-IRES-GFP-human-*CD226*$^{K295A+K333A}$ | synthesized and cloned by BioMatik, Cambridge, Ontario, Canada | this paper |
| pCL-Eco (retroviral packaging plasmid) | Kind gift from A/Prof Steven Lane, QIMR Berghofer, Brisbane, Australia | Addgene #12371 |
| PMD.2G (lentiviral envelope plasmid) | Kind gift from A/Prof Steven Lane, QIMR Berghofer, Brisbane, Australia | Addgene #12259 |
| px330-U6-Chimeric BB-CBh-hSPCas9 | | Addgene #42230 |
| pCAS9-mCherry-Frame +0 | Kind gift from Veit Hornung, (LMU, Munich, Germany) | Addgene #66939 |
| pCAS9-mCherry-Frame +1 | Kind gift from Veit Hornung, (LMU, Munich, Germany) | Addgene #66940 |
| pCAS9-mCherry-Frame +2 | Kind gift from Veit Hornung, (LMU, Munich, Germany) | Addgene #66941 |
| pCRISPaint-mNeon-PuroR | Kind gift from Veit Hornung, (LMU, Munich, Germany) | (Schmid-Burgk et al., 2016) |
| pNIC-CTHF- CBLB | Kind gift from Nicola Burgess-Brow, (University of Oxford, Oxford, UK) | Addgene #39056 |
| Software and Algorithms | | |
| R (v 3.6.3) | R Development Core Team, 2008 | https://www.r-project.org/ |
| R Studio (v 1.2.5033) | N/A | https://www.rstudio.com/ |

(*Continued on next page*)

*Continued*

| REAGENT or RESOURCE | SOURCE | IDENTIFIER |
|---|---|---|
| GraphPad Prism (v 7.0) | GraphPad Software, Inc | https://www.graphpad.com |
| FlowJo (v 10) | FlowJo LLC | https://www.flowjo.com |
| IDEAS (v 6.2) | Amnis, EMD Milipore | www.https://www.luminexcorp.com/imaging-flow-cytometry/ |
| Inkscape (v 0.92) | N/A | https://inkscape.org |
| Spotfire Analyst (v 7.6.1) | Tibco | https://www.tibco.com |
| inForm (v 2.2.1) | PerkinElmer | CLS135781 |
| ggplot2 (v 3.2.1) | (Wickham, 2016) | N/A |
| gplots (v 3.0.3) | (Warnes et al., 2019) | N/A |
| TCGAbiolinks (v 2.14.1) | (Colaprico et al., 2016) | N/A |
| SummarizedExperiment (v 1.16.1) | (Morgan et al., 2018) | N/A |
| Biobase (v 2.46.0) | (Huber et al., 2015) | N/A |
| Cgdsr (v 1.3.0) | (Jacobsen and Luna, 2019) | N/A |
| GenomicDataCommons (v 1.8.0) | (Morgan and Davis, 2019) | N/A |
| tSNE plots (v 1.4) | (Ashhurst 2017) | https://www.github.com/sydneycytometry |
| OutKnocker (v 1.31) | (Schmid-Burgk et al., 2014) | http://www.outknocker.org/ |
| Cutoff Finder (v 2.1) | (Budczies et al., 2012) | http://molpath.charite.de/cutoff/load.jsp |
| fgsea (v 1.12.0) | (Sergushichev 2016) | N/A |
| biomaRt (v 2.42.1) | (Durinck et al., 2005; Durinck et al., 2009) | N/A |
| GSEABase (v 1.48.0) | (Martin 2011) | N/A |
| remedy (v 0.1.0) | (Fay et al., 2018) | N/A |
| rstudioapi (v 0.11) | (Ushey et al., 2020) | N/A |
| cowplot (v 1.0.0) | (Wilke, 2019) | N/A |
| gridExtra (v 2.3) | (Auguie, 2017) | N/A |
| styler (v 1.3.2) | (Mueller and Walthert, 2020) | N/A |
| stringr (v 1.4.0) | (Wickham, 2019) | N/A |
| msigdbr (v 7.0.1) | (Dolgalev, 2019) | N/A |
| Seurat (v 3.1.5) | (Stuart et al., 2019) | N/A |
| dplyr (v 0.8.5) | (Wickham et al., 2020) | N/A |
| survminer (v 0.4.6) | (Kassambara et al., 2019) | N/A |
| survival (v 3.1-12) | (Herneau, 2020) | N/A |
| knitr (v 1.28) | (Xie, 2020) | N/A |
| EnhancedVolcano (v 1.5.4) | (Blighe et al., 2020) | https://github.com/kevinblighe/EnhancedVolcano |
| org.Mm.eg.db (v 3.10.0) | (Carlson, 2019) | N/A |
| CellRanger (v 3.0.2) | 10x Genomics, Pleasanton, CA, USA | N/A |

## RESOURCE AVAILABILITY

### Lead Contact

Further information and requests may be directed to, and will be fulfilled by the Lead Contact Tobias Bald (Tobias.Bald@qimrberghofer.edu.au).

### Materials Availability

Newly generated mouse strains, plasmids and cell lines are available upon request. Request may be directed to, and will be fulfilled by the Lead Contact Tobias Bald (Tobias.Bald@qimrberghofer.edu.au).

### Data and code Availability

The accession number for the scRNaseq data reported in this paper is European Genome-phenome Archive (https://www.ebi.ac.uk/ega/): EGAS00001004423. All Codes used in analysis can be found at https://github.com/BaldLab.

## EXPERIMENTAL MODEL AND SUBJECT DETAILS

### Mice

Wild-type (WT) C57BL/6 were purchased from Walter and Eliza Hall Institute for Medical Research or bred in house at QIMR Berghofer Medical Research Institute or Institute de recherches cliniques de Montréal animal facility. C57BL/6 *Cd226*$^{Y319F}$ mice (Zhang et al., 2015) were bred in-house and maintained at the QIMR Berghofer Medical Research Institute or Institute de recherches cliniques de Montréal animal facility. C57BL/6 Pmel-1 TCRtg GFP mice (Glodde et al., 2017), C57BL/6 CD226-deficient (*Cd226*$^{-/-}$) mice (Gilfillan et al., 2008), C57BL/6 *Cd226*$^{-/-}$.*Pmel-1* TCRtg GFP mice, C57BL/6 *Cd226*$^{-/-}$.*Pmel-1* TCRtg mice, C57BL/6 *Cd226*$^{Y319F}$.*Pmel-1* TCRtg GFP mice and C57BL/6 CD155-deficient (*Cd155*$^{-/-}$) (Li et al., 2018) mice were bred in-house and maintained at the QIMR Berghofer Medical Research Institute animal facility. Cbl-b "knock-in" mice (C373A; *Cbl-b*$^{4R}$) were obtained from the University of Western Australia (Oksvold et al., 2008). Mice greater than 6 weeks of age were sex-matched to the appropriate models. The number of mice in each group treatment or strain of mice for each experiment is indicated in the figure legends. In all studies, no mice were excluded based on pre-established criteria and randomization was applied immediately prior to treatment in therapy experiments. Experiments were conducted as approved by the QIMR Berghofer Medical Research Institute Animal Ethics Committee.

### Cell lines

Mouse B16F10 (melanoma) (originally obtained from ATCC), B16F10$^{ctrl}$, B16F10$^{Cd155-/-}$ (Li et al., 2018), MC38 (colon adenocarcinoma), MC38-OVA$^{dim}$, MC38-OVA$^{hi}$ (Gilfillan et al., 2008), HEK293T (kind gift from A/Prof Steven Lane, QIMR Berghofer, Brisbane Australia), Hepa 1-6 (hepatocellular carcinoma) (kind gift from Prof Greg Anderson QIMR Berghofer, Brisbane Australia), and RM-1 (prostate carcinoma) (Blake et al., 2016) cells were grown in Dulbecco's Modified Eagle Medium (DMEM; GIBCO) supplemented with 10% Fetal Calf Serum (FCS; Cell Sera), 1% glutamine (GIBCO), 1% sodium pyruvate, 1% non-essential amino acids (GIBCO), 100 IU/mL Penicillin, and 100 μg/mL Streptomycin (GIBCO). Mouse LWT1 (melanoma) (Ferrari de Andrade et al., 2014), RMA-S and its derivates (lymphoma) (Putz et al., 2017; Zhang et al., 2015), HCmel12-Pmel$^{KO}$-Tyrp1-Scarlett-hgp100 (HCmel12$^{hgp100}$) (melanoma) (Effern et al., 2020) and Jurkat (human T cell lymphoma) cells (clone E6.1) were cultured in "complete RPMI medium" consisting of RPMI-1640 (GIBCO) supplemented with 10% FCS (Cell Sera), 1% glutamine (GIBCO), 1% sodium pyruvate, 1% non-essential amino acids (GIBCO), 100 IU/mL Penicillin, and 100 μg/mL Streptomycin (GIBCO). CHO derived cell lines were cultured in CHO complete medium (Thermo Fisher) supplemented with 4% glutamine (GIBCO) and 2% Hypoxanthine, Thymidine (Corning). B16F10 and its variants, HCmel12$^{hgp100}$, RM-1, RMA-S and it derivates, LWT1 and Jurkat cell lines were maintained at 37°C, 5% $CO_2$. All MC38-derived cell lines were maintained at 37°C, 10% $CO_2$. CHO derived cell lines were maintained at 37°C, 8% $CO_2$ at 125 rpm. All cell lines were routinely tested negative for Mycoplasma, but cell line authentication was not routinely performed.

### Primary cell cultures

For *in vitro* studies single cell suspensions of bone marrow cells and/or lymphocytes isolated from mouse spleens or human PBMCs were cultured in "complete RPMI medium" (as described above) supplemented additionally with 1mM HEPES (GIBCO), and 50 μM 2-mercaptoetanol (Sigma) at 37°C, 5% $CO_2$.

### Patients and healthy donor specimens

All procedures involving human participants had approval from both the QIMR Berghofer Medical Research Institute Human Research Ethics Committee (HREC) (EC00278) and Royal Brisbane and Women's Hospital HREC (EC00172) and this study conformed to the Declaration of Helsinki. All tissue and blood samples were collected after obtaining written informed consent in accordance with participating hospitals/research institute Human Research Ethics Committee procedures and guidelines.

#### *HNSCC specimens*

HNSCC specimens were received from the Metro North HHS, Royal Brisbane and Women's Hospital, Brisbane, Australia. Fresh samples were processed using a commercially available Tumor Dissociation Kit (Miltenyi) including a tissue disaggregation platform (GentleMACS, Miltenyi) both according to the manufacturer's protocol. Peripheral blood mononuclear cells (PBMC) were isolated by Ficoll density gradient centrifugation from blood samples taken from the patient at the time of tumor excision. PBMC and tumor single-cell suspensions were then cryopreserved until further usage. Cryopreserved samples were thawed and incubated in RPMI 1640 containing 10 μg/mL DNase I (Sigma) and incubated at 37°C for 1 h to eliminate clumping and debris. The T cell stimuli used were 5 μL of anti-CD3 and anti-CD28 microbeads (Dynabeads, ThermoFisher Scientific) at approximately 2 × $10^5$ cells/well in RPMI 1640 (GIBCO) plus 10% FCS (Cell Sera), cultured at 37°C, 5% $CO_2$ for 4 h prior to staining for flow cytometry.

#### *Discovery cohort*

Archival formalin-fixed paraffin-embedded (FFPE) tissue specimens were obtained from pre-treatment patients with radiologically confirmed non-lymphoid stage IV melanoma (AJCC) from the Melanoma Institute Australia (MIA) as tissue microarrays from tumor core and tumor margins. Patient demographics and immunotherapeutic interventions are listed in Table S1. All patients received PD1 based immunotherapy between January 2015 and May 2018 and had provided written informed consent for the use of samples according to the institutional regulations. Pathology reports from all patients treated with immunotherapy were reviewed. Cases were selected for inclusion if there was sufficient archival FFPE tissue and clinical annotation for analysis.

### Validation cohort

#### *St. Gallen melanoma specimens*

Archival formalin-fixed paraffin-embedded (FFPE) tissue specimens were obtained from pre-treatment patients with confirmed unresectable stage IV melanoma (AJCC) from 4 different centers in Switzerland (Kantonsspital St. Gallen, Spital Grabs, Spital Wil, and Spital Flawil) from July 1st 2016 to December 31st 2018. Patient demographics and immunotherapeutic interventions are listed in Table S1. The study (Project ID 2016-009918) was approved by the Ethics Committee of Eastern Switzerland (Ethikkommission Ostschweiz [EKOS] 16/079) and conducted in accordance with the Declaration of Helsinki guidelines. All patients provided a written informed consent. Patients were treated either with antibodies against the checkpoint inhibitor molecule PD-1 (Pembrolizumab or Nivolumab) or in combination with an antibody against CTLA-4 (Ipilimumab).

#### *Bonn melanoma specimens*

Archival formalin-fixed paraffin-embedded (FFPE) tissue specimens were obtained from pre-treatment patients with confirmed stage IV melanoma (AJCC) from the Department of Dermatology from the University Hospital of Bonn as tissue microarrays from tumor margins. Patient demographics are listed in Table S1. All patients received PD1-based immunotherapy between January 2015 and August 2018 and had provided written informed consent for the use of samples according to the institutional regulations. Cases were selected for inclusion if there was sufficient archival FFPE tissue and clinical annotation for analysis.

## METHOD DETAILS

### In Vivo tumor models

#### *Subcutaneous and intraperitoneal tumor models*

For primary tumor growth experiments, MC38 and its variants ($1 \times 10^6$), B16F10 and its variants ($1 \times 10^5$), Hepa 1-6 ($2 \times 10^6$), and HCmel12$^{hgp100}$ ($2 \times 10^5$) cells were s.c. injected into mice in a final volume of 100 μL (day 0). Digital callipers were used to measure the perpendicular diameters of each individual tumor. The tumor size was calculated and is presented as mean ± SEM. When tumors reached a size of 150 mm$^2$ mice were sacrificed. For intraperitoneal tumor growth experiments, mice were injected with RMA-S ($1 – 5 \times 10^4$) tumor cells in in a final volume of 200 μL (day 0). Mice were observed for development of ascites and tumor growth for up to 100 d.

#### *MCA-induced carcinogenesis*

For 3-methylcholanthrene (MCA; Sigma) carcinogen-induced fibrosarcoma, male mice of the indicated genotypes were injected subcutaneously with 5 μg or 25 μg MCA in 100 μL sterile corn oil and development of fibrosarcoma was monitored.

#### *Experimental Metastasis*

For primary metastases B16F10 melanoma ($1 \times 10^5$ cells), LWT1 melanoma ($5 \times 10^5$ cells) or RM-1 prostate carcinoma ($1 \times 10^4$ cells) were injected intravenously. The metastatic burden was quantified in the lungs 14 days after injection by counting colonies on the lung surface as described previously (Blake et al., 2016).

#### *Vk*MYC myeloma transplant model*

The transplantable Vk*MYC myeloma cell line Vk12598 was maintained and expanded as previously described (Nakamura et al., 2018). Vk12598 MM cells ($5 \times 10^5$) were injected i.v. into the tail vein of mice. Survival was monitored daily and mice were euthanized when they developed signs of paralysis and reduced mobility.

#### *Adoptive Cell Transfer (ACT)*

ACT was performed as previously described with slight abbreviations (Glodde et al., 2017). When s.c. transplanted Hcmel12$^{hgp100}$ melanomas reached a size of > 5 mm in diameter mice were preconditioned by a single i.p. injection of 2 mg (~100 mg/kg) cyclophosphamide (Baxter) in 100 μl PBS followed by intravenous delivery of 1-2 × 10$^6$ hgp100-speciðc CD8$^+$CD90.1$^+$Pmel-1 T cells (in 200 μl PBS) the next day. Pmel-1 T cells were either from spleens from indicated genotype or derived from *in vitro* culture shortly (< 8 days) after retroviral transduction (see below). 50 μg of CpG 1826 (Biomers) and 50 μg of polyinosinic:polycytidylic acid (poly(I:C); Invivogen) in 100 μl PBS were injected peritumorally three times every 48-72 h after adoptive Pmel-1 T cell transfer and tumor growth and survival was monitored.

#### *Immune checkpoint- or CD226-blockade experiments*

For MC38-OVA$^{dim}$ tumors therapeutic blockade of PD-1 was performed on day 10, 14, 18 and 22 after s.c. tumor cell injection by i.p. injections of 250 μg rat anti-mouse PD-1 IgG2a (clone RMP1-14; BioXcell) or rat-control IgG2a mAb (clone 1-1; Leinco) in 100 μl PBS. For B16F10, therapeutic blockade of PD-1 and CTLA-4 was performed on days 6, 9, 12 and 15 after s.c. tumor cell injection using i.p. injections of 250 μg rat anti-mouse PD-1 IgG2a (clone RMP1-14; BioXcell) and 250 μg hamster-anti-mouse CTLA-4 IgG2a (clone UC10-4F10-11; BioXcell) or rat-control IgG2a mAb (clone 1-1; Leinco) resp. control-hamster IgG (BioXcell) in 100 μl PBS. For Hepa 1-6 tumors therapeutic blockade of PD-1 was performed on day 8, 11, 14, and 17 after s.c. tumor cell injection by i.p. injections of 50 μg rat anti-mouse PD-1 IgG2a (clone RMP1-14; BioXcell) or rat-control IgG2a mAb (clone 1-1; Leinco) in 100 μl PBS. For Hepa 1-6 tumors blockade of CD226 was performed on day 7, 8, 15, and 22 after s.c. tumor cell injection by i.p. injections of 250 μg rat anti-CD226 IgG2a (clone 480; produced in house) or rat-control IgG2a mAb (clone 1-1; Leinco) in 100 μl PBS.

### Tissue processing

Tumors and peripheral lymphoid tissues were processed using standard protocols. Briefly, tumors or lymphoid organs were harvested from mice and dissociated using GentleMACS Homogenizer (Miltenyi) as per manufacturer's instructions followed by incubation with 1 mg/mL Collagenase D (Sigma) and 1 mg/mL DNaseI (Roche) in "complete RPMI medium" at 37°C. After 30-45 min. tissues were passed through 70 μm cell strainers (Greiner) and further analyzed.

### Flow cytometry

Immunostaining of single-cell suspensions was performed according to standard protocols. Single cell suspensions were stained with fluorochrome-conjugated monoclonal antibodies listed in the Key Resource table in the presence of anti-CD16/CD32 (clone 2.4G2; produced in-house) in phosphate-buffered saline (PBS) containing 2% (v/v) FCS (Cell Sera) and 2.5 mM EDTA (Sigma). For OVA-Tetramer staining single kb-OVA biotinylated monomers were purchased from Prof Andrew Brooks, Department of Microbiology and Immunology, Peter Doherty Institute, University of Melbourne, Melbourne, Australia and stored at −80°C. For Tetramerization Streptavidin-APC (Biolegend) was added six times every 10-15 min until a 1:1.7 = Monomer:SA-APC ratio was reached. Assembled Tetramer was used within days. Tetramer staining was performed for 30' on ice. For intracellular cytokine staining of IFN-γ and TNFα single cells suspensions were cultured and or and not restimulated *in vitro* in "complete RPMI medium" at 37°C, 5% $CO_2$ in the presence of GolgiPlug (BD) or Cell Stimulation Cocktail (plus protein transport inhibitors; eBioscience) for 4-5 h and then surface stained as aforementioned. Surface stained cells were then fixed and permeabilized using BD Cytofix/Cytoperm (BD) according to the manufacturer's protocol and stained with anti-mouse IFN-γ (clone XMG1.2; Biolegend) or TNFα (clone MP6-XT22; Biolegend). For intranuclear staining single-cell suspensions were stained with antibodies against cell-surface antigens as aforementioned, fixed and permeabilized using FoxP3 Fix/Perm Buffer Kit (Biolegend) followed by intranuclear staining. Cells were acquired on the BD LSR Fortessa Flow Cytometer (BD Biosciences), CytoFLEX (Beckman Coulter) or Cytek Aurora Flow Cytometer (Cytek). Analysis was carried out using FlowJo V10 software (FlowJo, LLC). tSNE analysis of concatenated samples was performed in FlowJoV10.2 after appropriate down sampling to the indicated number and R based "tSNE plots" script was used for visualization.

### Cytokine Bead Array

Tumor single-cell suspensions were resuspended in an equal volume of "complete RPMI medium" and incubated for 4-5 h at 37°C, 5% $CO_2$ followed by supernatant collection. The supernatant was stored at −80°C until analysis using Cytokine Bead Array (BD) using manufacturer's protocol.

### Generation of CRISPitope-engineered cell line (HCmel12$^{hgp100}$)

HCmel12$^{hgp100}$ cell lines were generated as described previously (Effern et al., 2020). Briefly, a stable knock-out of the *Pmel* gene in HCmel12 melanoma cells was generated by targeted CRISPR/Cas9. HCmel12 cells were transfected with px330-U6-Chimeric_BB-CBh-hSPCas9 (Addgene #42230) plasmid encoding a double-stranded DNA oligonucleotide targeting upstream of the genomic region encoding for the pmel-1 T cell epitope in exon 1 of the murine *Pmel* gene. Genomic aberrations of *Pmel*-knockout single cell clones were characterized by next generation sequencing and analyzed using the web tool OutKnocker (Schmid-Burgk et al., 2014). The plasmid px330-U6-Chimeric_BB-CBh-hSPCas9 was used as target selector. A double-stranded DNA oligonucleotide targeting the C terminus of the desired target gene was cloned into the BbsI-digested px330 to generate a functional sgRNA. Frame selectors pCAS9-mCherry-Frame +0, pCAS9-mCherry-Frame +1 and pCAS9-mCherry-Frame +2 were a gift from Veit Hornung (LMU, Munich, Germany; Addgene #66939, #66940 and #66941). Universal donor plasmids were cloned based on the pCRISPaint-mNeon-PuroR plasmid described previously (Schmid-Burgk et al., 2016). The universal donor pCRISPaint-mNeon-PuroR was a gift from Veit Hornung (LMU, Munich, Germany). Using molecular cloning approaches, the pCRISPaint-mNeon-PuroR plasmid was further modified by (1) exchanging the Puromycin resistance cassette by a Blasticidin resistance cassette, (2) exchanging the Methionine start codon (ATG) of the resistance cassettes by a Glycine (GGG) to prevent transcription from random genomic integrations, (3) exchanging the mNeon fluorescent protein by the mScarlet fluorescent protein, and (4) addition of a FLAG-tag and the human gp100 epitope ($aa_{25-33}$: KVPRNQDWL) to the fluorescent protein (C terminus). CRISPitope-engineered HCmel12 melanoma cells were generated by targeting the C-termini of the Pmel gene by CRISPR-assisted insertion of epitopes. For CRISPitope plasmid transfection, 50.000-100.000 HCmel12-gp100 knock out cells were seeded in a 96-well plate and transfected with 200 ng of DNA (50 ng target selector, 50 ng frame selector and 100 ng universal donor) in Opti-MEM I (Life Technologies) using 0.6 μl of Fugene transfection reagent (Promega) according to the manufacturer's instructions. After selection, CRISPitope-engineered cell lines were sorted for mScarlet expression using a FACS Aria III high-speed cell sorter (BD) and subsequently polyclonal cultures of the individual cell lines were established.

### Transduction of mouse CD8$^+$ T cells

Full-length mouse CD226 cDNA sequence was synthesized and separately cloned (BioMatik) into the MSCV-IRES-GFP plasmid (kind gift from A/Prof Steven Lane, QIMR Berghofer, Brisbane, Australia; Addgene #20672). For generation of retrovirus, HEK293T cells were plated on 10 cm dishes overnight at a concentration of 4 × $10^6$ cells/dish. The following day, packaging plasmid pCL-Eco (kind gift from A/Prof Steven Lane, QIMR Berghofer, Brisbane, Australia) and plasmid encoding either MSCV-IRES-GFP-*Mock* or MSCV-IRES-GFP-*CD226 WT-full-length* were mixed along with Fugene 6 (Promega) as per the manufacturer's protocol at a 3:1 = Fugene:DNA ratio and applied to the HEK293T cells overnight. Medium was then replaced and viral supernatant was collected twice in the following 48 h. Retroviral supernatants were spun for 2-6 h at 17.000 *g* for virus concentration and immediately stored at −80°C. For transduction, CD8$^+$ T cells were plated at 1-3 x$10^6$ per well in 6-well plates that had been coated overnight in 5 μg/mL Retronectin (Takara Bio Inc.) and viral supernatant in a 1:1 vol/vol ratio and 4 μg/mL Polybrene (Sigma) was added. Spinfection was performed at 30°C for 2 h at 2000 g with no acceleration or brake. Media was replaced after 2-4 h. In some experiments, spinfection was repeated after 24 h. Cells were maintained in 100 IU/mL human IL-2 (Novartis) and 2 ng/mL mouse IL-7 (Biolegend) and checked for purity until used in experiments and ACT.

### T cell stimulation assays

For mouse T cell stimulation, splenocytes or MACS enriched $CD8^+$ T cells (Stemcell) of indicated genotype were stimulated in round-bottom 96-well plates using stimulation beads which were generated using the Dynabeads® M-270 Epoxy bead coupling kit acc. to manufacturers protocol with anti-CD3 (clone 145-2C11), anti-CD28 (clone) and, if indicated, CD155-Fc (Sino Biological) at 5μg/mg Beads. Beads were used at concentrations from 0.1 – 1) μl/well at 1-2 × $10^5$ cells/well for the time indicated. When indicated, a small molecule inhibitor or DMSO as vehicle control was present during the assay. In case of MG132, PitStop2 and Dynasore, lymphocytes were preincubated for 15-30 min before stimulation.

### NK cell stimulation assays

IL-2 activated primary mouse NK cells from either WT or *CD226*$^Y$ mice or human YT-S NK cells ectopically expressing mouse CD226 were co-cultured with equal number of RMA-S cells (expressing or not mouse (m) CD155) for 4 h or the times indicated. CD226 expression was then determined via flow cytometry. When indicated the small molecule inhibitor PP2 (Millipore) was present at indicated concentrations during the assay.

### CD226 internalisation assay

MACS purified $CD8^+$ T cells (Stemcell) of the indicated genotype were stimulated with soluble anti-CD3 (clone 145-2C11; 1 μg/mL) and soluble anti-CD28 (clone 37.51; 1 μg/mL) antibodies in "complete RPMI medium" supplemented with 20 IU/mL human IL-2 (Novartis) for 48 h at a concentration of 1-2 × $10^6$ cells/mL. Cells were then seeded in a flat-bottom 96-well plate which was coated overnight at 4° with hIgG1 (IgG; BioXcell; 0.3 μg/well) or recombinant mCD155 fused to the carboxy-terminal Fc region of human IgG1 (CD155-Fc; Sino Biological; 0.3 μg/well). After 1 h incubation at 37°C, 5% $CO_2$ cells were harvested and surface stained for $CD8^+$ (BV421; clone 53-6.7; Biolegend) and CD226 (AF647; clone 10E5; Biolegend) followed by fixation, permeabilization. Clone 10E5 blocks binding of clone 480.1, which was used for following intracellular stain of CD226 (PE; clone 480.1; Biolegend). Cells were then immediately acquired on a four laser, 12 channel Amnis ImageStream$^X$ *MkII* (Amnis, EMD Millipore, Seattle, WA, USA) at a x60 fold magnification at low speed. Data analysis was performed using IDEAS software (Amnis). The gating strategy for analysis involves the selection of cells in focus based on "gradient RMS." Cells with high "Aspect ratio" and low "Area" values were selected as they are likely singlets and subjugated on $CD8^+$ (BV421) cells. Good quality, focused and centered cells were selected and at least 100 cells per group were analyzed.

### Analyses of immunological synapse formation

Synapse formation assay was performed as previously described (Markey et al., 2015) with minor modifications. Bone marrow derived dendritic cells were prepared by flushing the long bones from the hind legs of sacrificed mice of the indicated genotype. Cells were seeded at 1-3 × $10^6$ cells/mL in "complete RPMI medium" supplemented with 1 ng/mL mouse GM-CSF. After three-four days non-adherent cells were collected and further cultured. Experiments were performed after at least seven days of *in vitro* differentiation. The day before the assay BMDC were harvested and labeled with Cell Trace Violet (CTV; Life Technologies) as per the manufacturer's instructions and overnight peptide-loaded with 1 μg/mL H2-$D^b$ binding peptide $hgp100_{25\text{-}33}$ peptide (KVPRNQDWL; Mimotopes). On the same day, $CD8^+$ T cells of the indicated genotype were isolated using MACS technology (Miltenyi) according to the manufacturer's instruction from single-cell suspensions of spleens and plated at 1 × $10^6$ cells/mL in 10-20 U hIL-2 (Novartis). The next day, T cells were harvested and CFSE (Biolegend) labeled as per the manufacturer's protocol. BMDC and T cells were then co-cultured at a 1:2 or 1:3 = T:DC ratio for ~1 h at 37°C, 5% $CO_2$. At the end of incubation period cells were fixed with 3 x volume 1.5% Paraformaldehyde at room temperature, followed by surface stain of LFA-1 (PE-Cy7; clone H155-78; Biolegend) in the presence of anti-CD16/CD32 (clone 2.4G2; produced in-house) in PBS containing 2% (v/v) FCS (Cell Sera). Following surface staining, cells were washed and permeabilized using 100 μL of 0.1% Triton-X (Sigma). 3 μL of phalloidin (AlexaFluor 647; Life Technologies) was added to each sample, and cells were incubated for 30 min at room temperature. During the whole staining process, cells were treated extremely carefully and vortexing, thorough resuspending, or EDTA was deliberately avoided to maintain established synapse formations. At the end of the staining period, cells were washed and immediately acquired on a four laser, 12 channel Amnis ImageStream$^X$*MkII* (Amnis) at a x60 fold magnification at low speed. Data analysis was performed using IDEAS software (Amnis). The gating strategy for analysis involves the selection of cells in focus based on "gradient RMS." Cells with intermediate "Aspect ratio" and intermediate "Area" values were selected as they are likely doublets. We subgated on double-positive $CTV^+$ and $CFSE^+$ "events." Finally, good quality, focused and centered were selected. The interface mask was applied and the T cell defined as the target of interest. The fluorescence intensity of LFA-1 and Phalloidin within the Interface mask serves as a surrogate marker for the strength and intensity of the immunological synapse. Statistical significance was determined using Kruskal-Wallis one-way analysis of variance with Dunn's test for multiple comparisons.

### Transduction of Jurkat cells

Full-length human $CD226^{WT}$ and $CD226^{K295A+K333A}$ cDNA sequences were synthesized and cloned (BioMatik) into the MSCV-IRES-GFP plasmid. For generation of retrovirus, HEK293T were transfected with Fugene 6 (Promega) with envelope pMD2.G (Addgene plasmid #12259) and packaging pCL-Eco plasmid encoding and appropriate transfer plasmid. Medium was then replaced and viral supernatant was collected twice in the following 48 h. Retroviral supernatants were spun for 2-6 h at 17.000 *g* for virus concentration and stored at −80°C or used immediately. For transduction, Jurkat cells were plated at 1 × $10^6$ cells per well in 24-well plates that had

been coated overnight in 5 μg/mL Retronectin (Takara Bio Inc.) and viral supernatant in a 1:1 vol/vol ratio and 4 μg/mL Polybrene (Sigma) was added. Spinfection was performed at 30°C for 2 h at 2000 g with no acceleration or brake. Media was replaced after 2-4 h.

### Human T cell bead-stimulation assays

PBMCs were thawed and treated with DNase I (Roche) to remove dead cells prior to culture. 1 × $10^5$ PBMC were cultured in RPMI-1640 (GIBCO) + 10% FCS (Cell Sera) in 200 μL volume in U-bottom 96-well plates. T cell activation was achieved by the addition of 2 × $10^5$ CD3/CD28 stimulator beads (Thermo Fisher Scientific). The culture was incubated at 37°C, 5% $C0_2$. At the completion of the culture period, the cells were stained for surface markers and analyzed by flow cytometry.

### Generation of OKT3+/– CD155 expressing CHO cells

Human *PVR* (NM_006505, NP_006496) was sub-cloned from R&D Systems RDC1289 into pLenti-EF1a (Origene). Lentivirus was produced using the Lenti-X Single Shot packaging system according to the manufacturer's instruction (Clontech). CHO-OKT3 (Subclone 2E5; Immuno-Oncology Discovery, Bristol-Myers Squibb) cells were transduced with polybrene (Sigma; 5μg/mL) and sorted for CD155 expression levels.

### hCD226-CD155 interaction using artificial APC

Ficoll processed and enriched $CD3^+$ T cells using RosetteSep (Stemcell) or MACS enriched $CD8^+$ T cells from HD PBMCs or bulk HD PBMCs or Jurkat cells and its derivates were stimulated with CHO-OKT3 or OCH-OKT3-CD155 cells at various ratios (CHO: T cell = 1:1 - 1:20) for indicated times. In some experiments, a small molecule inhibitor or DMSO as vehicle control was present during the assay. In case of MG132, PitStop2 and Dynasore, T cells were preincubated for 15-30 min before stimulation with indicated CHO cells. In some experiments, pre-activation of $CD8^+$ T cells was performed for 7 to 10 days in ''complete RPMI medium'' supplemented with 25 μL/mL of anti-CD3/CD28 tetrametric antibody (Stemcell) and 80 IU/mL of human IL-2 (PeproTech). For CD155 blockade, titrated anti-human CD155 antibody (clone SKII.4, Biolegend) were pre-incubated with CHO cells at indicated dosage for 30 min prior to co-culture with human T cells. For immunoblot analysis cell were re-isolated using MACS $CD8^+$ positive selection (Miltenyi) before cell lysis.

### Immunoblot

Immunoblots were performed as previously described (Möller et al., 2009). Briefly, cells were lysed in RIPA buffer supplemented with cOmplete™ Protease Inhibitor Cocktail (Roche). Protein content was quantified using a BCA Protein Assay kit (Sigma). All samples were reduced by boiling at 95°C for 5 min in SDS sample buffer containing 5% beta-mercaptoethanol (Sigma). Equal amounts of total protein were then loaded onto hand cast polyacrylamide gels. Proteins were resolved by SDS-PAGE and transferred to PVDF membranes (Bio-Rad), which were probed with the following antibodies: mouse anti-ubiquitin (clone Ubi-1, Invitrogen); rabbit anti-human CD226 (clone 102, Sino Biological); rabbit anti-mouse CD226 (clone EPR20710, abcam); mouse anti-Cbl-b (clone G-1, Santa Cruz Biotechnology); rabbit anti-β-actin (polyclonal, Cell Signaling Technology); and mouse anti-α-tubulin (clone DM1A, Sigma). Membranes were further probed with the following HRP-conjugated secondary antibodies: goat anti-rabbit IgG (polyclonal, Invitrogen); and goat anti-mouse IgG (polyclonal, Invitrogen). Protein bands were detected using enhanced chemiluminescence reagent (Amersham ECL Select, GE Healthcare), and visualized on ChemiDoc Touch Imaging System (Bio-Rad).

### Immunoprecipitation of CD226

Cells were lysed in TOTEX buffer (0.35 M NaCl, 1 mM MgCl2, 0.5 mM EDTA, 0.1 mM EGTA, 20% glycerol, 1% NP-40, 0.5 mM DTT, 20 mM HEPES, pH7.9) supplemented with cOmplete™ Protease Inhibitor Cocktail (Roche). Total protein extracts were incubated with anti-CD226 antibody (1 μg) for 1 h at 4þC under agitation, and further incubated with Protein A/G agarose beads (Protein A/G PLUS-Agarose Immunoprecipitation Reagent, Santa Cruz Biotechnology) overnight at 4þC under gentle agitation. Beads conjugated with immune-captured samples were washed 5 times with PBS. To elute proteins from the beads, samples were incubated with 20 μL of SDS sample buffer containing 5% beta-mercaptoethanol (Sigma) at 95°C for 10 min. Protein content in the supernatant was finally analyzed by immuno blotting as aforementioned.

### CBL-B TKB-Protein production

The CBL-B TKB expression vector pNIC-CTHF encodes the TKB domain of CBL-B (*CBLB*) fused to a C-terminal Tobacco Etch Virus (TEV) protease A cleavage site followed by hexahistidine and FLAG tags, and was a gift from Nicola Burgess-Brown (Addgene plasmid #39056). The *CBLB* construct was transformed into *E. coli* BL21(DE3) cells, which were grown in Super Broth at 37°C to an $OD_{600}$ 0.6. Protein expression was induced with 1 mM isopropyl β-D-1-thiogalactopyranoside (IPTG) for 18 h at 18°C. Cells were harvested by centrifugation and lysed by sonication in 50 mM HEPES pH 7.5, 500 mM NaCl, 5% glycerol, 5 mM imidazole, supplemented with Complete Protease Inhibitor Cocktail Tablets (Roche). Soluble fusion protein was affinity-purified using nickel-Sepharose resin (Ni Sepharose® 6Fast Flow; GE Healthcare), under gravity filtration and eluted using a stepwise imidazole gradient (30-250 mM). The hexahistidine and FLAG tag were cleaved overnight at 4°C using TEV protease. Cleaved protein was purified

by size exclusion chromatography using a HiLoad 16/60 S200 Superdex column (GE Healthcare) at 1.0 mL/min flow rate in 50 mM HEPES pH 7.5, 500 mM NaCl, 5% glycerol and 0.5 mM TCEP. The Cbl-b TKB domain was further purified by cation exchange chromatography using a 5 mL Mono S column (GE Healthcare).

### Surface Plasmon Resonance (SPR)

All SPR experiments were conducted on a BIAcore400 instrument (GE healthcare) at 18°C. The binding affinity of CBL-B TKB domain to different phosphopeptides was analyzed by surface plasmon resonance competition. A biotinylated phosphotyrosine-containing peptide derived from ZAP70 (pY292; Biotin-GSGS-DGpYTPEPA) was immobilized to a Streptavidin coated SA chip (GE Healthcare). A reference flow cell was prepared by the same procedure in the absence of peptide. Increasing concentrations of competitor peptides (0.1 to 10 μM) pre-incubated with 100 nM *CBLB* were injected at a rate of 30 μl/mL in 10 mM HEPES pH7.4, 150 mM NaCl, 3.4 mM EDTA and 0.005% Tween 20. Maximal CBL-B binding was determined in the absence of competitor peptide. The surface was regenerated between injections with 50 mM NaOH, 1M NaCl at a flow rate of 30 μL/min for 20 s. Reference flow cell sensorgrams were subtracted from the ligand flow sensorgrams for all analyses. Relative binding values obtained using the BIAcore evaluation software (GE Healthcare) were plotted against $Log_{10}$ competitor peptide and a steady state analysis (one site-Fit $logIC_{50}$) was performed using Prism 8 (version 8.0.2) to derive $IC_{50}$ values.

### qPCR analysis

Isolated human $CD8^+$ T cells were immediately snap-frozen. Total RNA was isolated and purified using RNeasy columns (QIAGEN). RNA was reverse-transcribed using Superscript II and oligo-dT18 primers (Invitrogen). PCR was performed with a fast SYBR Green Master Mix (ABI) using CD226 and GAPDH primers as listed in the Key resource Table. CD226 gene expression was depicted using the ΔΔCT method.

### Gene expression analysis of human PBMCs

Isolated PBMCs from healthy donors were plated onto 48-well plate at $0.5 \times 10^6$ cells/well. The cells were stimulated for 48 h with or without suboptimal concentration of anti-CD3 (clone OKT3; BioLegend, 200 pg/mL) in the presence of isotype control (MOPC-21 mouse IgG1; BioLegend; 1 μg/mL) or anti-CD226 (clone DX11; BioLegend; 1 μg/mL). Stimulated cells were harvested and resuspended in 350 μL of RLT lysis buffer (QIAGEN). The lysed cells were frozen down immediately and sent to Core Diagnostics (Hayward, California) for Nanostring analysis.

### Generation and sequencing of single cell libraries

Single-cell and CD226-ADT libraries were generated from sorted live $CD8^+CD90.1^+$Pmel-1 T cells stained with an anti-CD226 TotalSeq antibody using the Single Cell 3¢ Library GEL kit v3 (10x-1000092, Decode Science) according to the manufacture's instructions. Following generation of single cell libraries, samples were diluted to 4 nM. RNA and CD226-ADT libraries generated from Pmel-1 T cells were pooled at 80% RNA, 10% ADT and 10% PhiX Control v3 Library. These pooled libraries were further diluted to 1.4 pM, then were denatured and loaded on a NextSeq550 at the Analytical Facility of the QIMR Berghofer Medical Research Institute. Samples were run using NextSeq 500/550 High Output v2 kits (150 cycles) with the following sequencing run parameters: Read 1: 28 cycles; i7 Index 8 cycles; Read 2: 91 cycles.

### NGS data analysis

Raw sequence files were converted to FASTQ files using illumina's bcl2fastq (v2.19.403) tool. These files were then processed using CellRanger (v 3.0.2) run on a high-performance cluster utilizing the Linux distribution CentOS7. For both single cell gene expression (TOBI070819) and antibody capture sequencing (CITETOBI070819) default CellRanger options were used to map reads and for count quantification. The transcriptome reference used was the mouse genome mm10 (CellRanger reference v 3.0.0). Reads were mapped for 1,936 cells with a median 2,365 genes per cell and a mean of 85,603 reads per cell for transcriptomic data. Protein expression data, a total of 864,298 reads were acquired resulting in a mean of 446 reads per cell.

Standard quality control and normalization, as part of the Seurat (v 3.1.5) pipeline (Stuart et al., 2019), were performed in R (v 3.6.3) on a MacBook Pro running Catalina (v 10.15.2). In brief, genes were removed if they were detected in less than 3 cells. Additionally, cells were excluded from further analysis if they had less than 200 or more than 6,000 genes or mitochondrial genes were greater than 5% of gene counts. Following filtering, the dataset contained 1,526 cells and 13,172 genes. The default settings recommended by Seurat were used for normalization of both protein and RNA expression data. Cells were then split into Cd226 high, dim, and neg populations based on Cd226 protein expression level. $Cd226^{hi}$ and $Cd226^{neg}$ cells represent the top and bottom 25% of expression whereas $Cd226^{dim}$ population consists of the middle 50%. For heatmap generation, the dataset was first down sampled to 300 cells per group. Where indicated imputed gene expression values were used for data visualization. Imputation was performed on all genes in the dataset using the RunALRA function in Seurat. Unless stated, all visualization was performed using default setting in Seurat. Volcano plot was generated using the EnhancedVolcano package (v 1.5.4) (Blighe et al., 2020) with genes depicted if they had an adjusted $p < 0.05$ and a $log_2$ fold change greater than 0.25 or less than −0.25. Gene ontology (GO) analysis was performed using clusterProfiler (v 3.14.3)(Yu et al., 2012), msigdbr (v 7.0.1)(Dolgalev, 2019), and org.Mm.eg.db (v 3.10.0)(Carlson, 2019) as outlined in the clusterProfiler pipeline.

### Immunohistochemical staining for human CD155

The TMA was sectioned at 3 μm on superfrost+ glass slides and stored under vacuum until IHC was performed. Slides were dehydrated at 65°C for 20 min, deparaffinized in xylene and rehydrated in graded ethanol. Antigen retrieval was performed in EDTA buffer (pH 9) in a Decloaking Chamber (Biocare Medical) at 100°C for 20 min. IHC was performed on an Autostainer-Plus (DAKO). The primary rabbit anti-human antibody against CD155 (D3G7H; CST) was incubated for 45 min at room temperature using a 1:100 dilution and visualized using the MACH3 Rabbit HRP polymer detection system (Biocare) and DAB Chromogen Kit (Biocare) as per the manufacturer's instructions. Slides were counterstained with diluted hematoxylin. CD155 was then evaluated as the percentage of membrane positive tumor cells and the maximum intensity of the immunohistochemical signal was recorded. CD155 expression was assigned using the H-score method and categorized as follows; score 1+ (0 - 99), score 2+ (100-199) or score 3+ (200 - 300).

### Multiplex immunohistofluorescence (mIHF) staining

Using above mentioned TMA and multispectral fluorescence imaging, we quantified the expression of CD226 on $CD8^+$ T cell in melanoma samples. SOX10 was used to identify melanoma cells and DAPI was used as a nuclear stain. Specimens were sectioned at 4 μm onto superfrost+ microscope slides and stored under vacuum until mIHF was performed. Heat-induced antigen retrieval with EDTA target retrieval buffer (DAKO) was performed using an antigen-decloaker at 100°C for 20 min and washed in Tris-buffered saline solution with Tween 20 (TBS-T) (pH 7.6). Staining was run on an automated tissue stainer (DAKO). Primary antibodies were visualized using the OPAL multiplex TSA detection system (PerkinElmer) as per the manufacturer's instructions with heating for 20 min at 100°C using EDTA buffer between sequential staining rounds to strip prior bound antibody/HRP complexes. Primary antibodies, were diluted in Van Gogh Yellow Diluent (Biocare) and incubated for 30 min, followed by a two-step polymer-HRP detection system (Biocare) and then labeled with TSA-based fluorophores (Opal Reagent Pack; PerkinElmer). The following primary antibodies/clones were used sequentially in the order listed with antibody dilutions and Opal-fluorophores listed in parenthesis: CD8/144b (1:1000; Opal570), CD226/102 (1:500; Opal520) and SOX10/BC34 (1:500; Opal690).

### Multiplex-IHF Image acquisition and analysis

Fluorescence-stained slides were scanned using a Vectra imaging system (PerkinElmer). Whole slide scanning was done at 4 × magnification using mixed fluorescence followed by 20 × multispectral imaging. Images were spectrally unmixed followed by tissue and cell segmentation using Inform analysis software (PerkinElmer; v2.2.1). Merged data files were processed, and fluorescence thresholds were set using Spotfire image-mapping tools (Tibco Spotfire Analyst; v7.6.1) followed by segmented cell counting using Spotfire. Stratification of patients into "high $CD226^+CD8^+/CD8^+$" (= CD226 ratio, CD226r) versus "low $CD226^+CD8^+/CD8^+$" or "high $CD8^+$" versus "low $CD8^+$" was determined using the "Cutoff Finder" tool (Budczies et al., 2012).

### The Cancer Genome Atlas (TCGA) transcriptomic analysis

Gene expression data (RNA-seq) of TGCA cancer cohorts was accessed and analyzed through the cBioportal for Cancer Genomics (http://www.cbioportal.org) using the R-based packages CGDS-R and TCGAbiolinks. Guidelines for the use of TCGA data (https://cancergenome.nih.gov/) were followed. We retrieved individual gene expression values for the genes of interest as RPKM normalized read counts.

### Moving average analysis

Moving average analysis was performed as previously published (Glodde et al., 2017; Riesenberg et al., 2015). In brief, TCGA data was accessed using the R package "cgdsr" (v 1.3.0). Samples were subsequently ordered by increasing expression values of *CD226*. The moving average of *CD8B, NCAM, IFNG, PVR, GZMB*, and *NECTIN2* gene expression in tumor tissues was calculated using a sample window size of n = 20. Correlation was calculated using non-parametric Spearman rank and statistical significance was determined by an asymptotic Spearman correlation test.

### Survival analysis of TCGA transcriptomic data

Harmonized (hg 38) gene expression data (RNA-seq) for select TCGA cancer cohorts was accessed via the R package TCGAbiolinks (v 2.14.1). Analysis was performed as per TCGAbiolinks standard pipeline. Hazard ratio was calculated using a proportional hazards regression model implemented with the survival package (v 3.1–12). Statistical significance was determined using a Likelihood ratio test.

## QUANTIFICATION AND STATISTICAL ANALYSIS

Statistical analyses were conducted with Graph Pad Prism 7 and 8 (GraphPad Software). If not stated otherwise, Student's t test was used for comparisons of 2 groups, One-way ANOVA for comparison of multiple groups with posthoc Tukey's test for multiple comparisons. Significance of *in vivo* experiments was calculated by log-rank (Mantel-Cox) test for Kaplan-Meier survival analysis or Two-way ANOVA with posthoc Tukey's test for multiple comparisons. A Fisher's exact test was used to determine the significance of the proportion of tumor free mice. Differences between groups are shown as the mean ± SD. P values of less than 0.05 were considered statistically significant. $p < 0.05$ = *; $p < 0.01$ = **; $p < 0.001$ = ***; $p < 0.0001$ = ****.